



UTRECHT UNIVERSITY

MASTER THESIS

First light from XAMS

**Electronic recoil calibration of the Netherland's first dual-phase
xenon time projection chamber**

Author:

Maria Karolina Margit BADER

Supervision by:

Prof. Dr. Patrick DECOWSKI

Dr. Auke-Pieter COLIJN

MSc. Erik HOGENBIRK

June 25, 2015

Contents

1	Motivation	3
2	Searching for dark matter	4
2.1	Evidence for dark matter	4
2.1.1	Galactic Rotation Curves	4
2.1.2	Galaxy Clusters	5
2.1.3	The Cosmic Microwave Background	7
2.2	Dark matter candidates	9
2.2.1	Axions	9
2.2.2	WIMPs - Weakly Interacting Massive Particles	10
2.3	Direct dark matter detection	11
2.3.1	Detection principles	11
2.3.2	Xenon as detector material	12
2.3.3	Dual-phase xenon time projection chambers	14
3	The XAMS setup	16
3.1	The dual-phase xenon time projection chamber	17
3.1.1	Teflon structure and electric fields of the time projection chamber	17
3.1.2	Scintillation light detection with photomultiplier tubes	19
3.1.3	The determination of the liquid level in the TPC during operation	20
3.2	Xenon gas recirculation and purification system	24
3.3	Liquifying xenon in the cooling tower	26
3.4	Monitoring the system: The detector slow control	27
3.5	The data acquisition and processing at XAMS	28
3.5.1	The V1730 CAEN digitizer and XENON1T readout software Kodac	29
3.5.2	Data processing and analysis	31
4	Collimator setup for the electronic recoil calibration of XAMS	33
4.1	The collimator working principle	33
4.2	Attenuation of γ -rays in the XAMS detector material	35
4.3	Geant4 Monte Carlo simulation of the collimator setup	37
5	Detector characterisation	39
5.1	Event selection for data analysis	39
5.2	Interaction depth and collimator beam width	40
5.3	Top-bottom asymmetry	41
5.4	S2 broadening	43
5.5	Electron lifetime	44
5.6	Light collection efficiency	46
5.7	S1 light yield	47
5.8	Combined energy scale	49
6	Conclusion and outlook	52

1 Motivation

The hunt for dark matter is one of the most intriguing challenges for the current generation of physicists. During the last decades, astrophysical observations wiped out any doubt that a new, non-baryonic type of matter must exist and that this new type of matter, called *dark matter*, is by far the most abundant type of matter of the universe. Despite its overwhelming abundance, dark matter has never been directly observed. As a result, many different experiments are currently competing to record the first, dark matter detection signal.

One of these experiments is the XENON experiment, which is installed 1400 m underground at the Laboratori Nazionali del Gran Sasso of INFN in Italy. Up to 2013, the XENON collaboration was operating the most competitive xenon dark matter detector: the XENON100 experiment. Currently, the commissioning of the next generation xenon dark matter experiment, the XENON1T detector, is taking place. For dark matter detection the collaboration deploys a terrestrial, large-scale, low-background dual-phase xenon time projection chamber. The detector operates with ultra pure liquid xenon, which emits two distinct types of signals as response to interactions with particles. These two signals allow to infer properties on the particles that pass through and interact with the detector material. By shielding the detector from background radiation, new types of matter can be identified.

The current R&D and software upgrades of XENON1T and the improvement of detection and analysis techniques for future XENON detectors rely on the findings of smaller-scale xenon experiments. One of these so called *demonstrators* is XAMS, the Netherlands first dual-phase xenon time projection chamber in Amsterdam. As part of the Dark Matter research group at the Nikhef institute, it currently contributes to the improvement of the data processing software for XENON1T. With an active detector mass of about 450 g, future studies will test alternatives for the currently deployed PMTs for light detection and contribute to the understanding of how light pulse shapes can be used to discriminate between different types of particles.

With this Master research, XAMS was brought to a fully operational and understood level from which further research contributing to the XENON experiment can be conducted. Chapter 2 of this thesis describes the evidences for the existence of dark matter. Chapter 3 elaborates on the design and construction of the XAMS facility and the XAMS dual-phase xenon time projection chamber, while Chapter 4 describes a collimator setup for the electronic recoil calibration. Chapter 5 shows the analysis and interpretation of the calibration data, confirming a working XAMS facility for detailed studies of xenon properties and detection principles.

2 Searching for dark matter

Since the last decade, there has been astonishing astronomical and cosmological evidence, that the energy density of our universe is dominated by two contributions that are barely understood. Data from the Planck mission revealed that the main contribution comes from dark energy, making up 68.3 % of the energy content of the universe. The second contribution comes from a new type of matter, the so called *dark matter*, that contributes with 26.8 % to the energy-mass content of the universe. The contribution of the ordinary, baryonic matter only accounts for 4.6 % of the total content of the universe [1].

Dark energy is an unknown type of energy that is responsible for the accelerated expansion of the universe. Dark matter is known to make up ~ 80 % of the non-relativistic matter contribution in the universe [2], which means that it is much more abundant in the universe than ordinary baryonic matter. Cosmological observations lead to the conclusion that this new type of matter only interacts extremely weakly with photons, resulting in the name *dark matter*. Until today the existence of dark matter has only been inferred by the gravitational influence it has on ordinary matter. No interaction of ordinary matter with dark matter has been observed yet, which leads to the hypothesis that this interaction is very weak. Nevertheless, current detection techniques are rapidly increasing in sensitivity and several experiments are currently running to search for the dark matter particle.

This chapter will give an introduction to the evidence for the existence of dark matter, it will introduce two compelling models for dark matter candidates and conclude with a description of dark matter detection methods.

2.1 Evidence for dark matter

The three most compelling cosmological and astrophysical observations that give evidence for the existence of dark matter are the rotation curves of spiral galaxies, galaxy clusters and the anisotropies in the cosmic microwave background. This chapter mainly follows [3].

2.1.1 Galactic Rotation Curves

The rotation curves of spiral galaxies are probably the most convincing evidence for dark matter. In the early 1970s it has been found that the measured galactic rotation curves, that is the curve describing the velocity of a star rotating around the centre of the galaxy depending on its distance from it, does not coincide with the rotation curves predicted by Newtonian mechanics. From simple Newtonian principles the rotational velocity can be calculated as:

$$v(r) = \sqrt{\frac{GM(r)}{r}}, \quad (1)$$

where G is the gravitational constant and $M(r)$ the amount of mass enclosed at a certain radius r . This means that at a radius beyond the stellar disc, where the amount of mass is negligible compared to the total mass of the galaxy, the rotational velocity should decrease with $v(r) \propto \frac{1}{\sqrt{r}}$.

Nevertheless, this is not what has been observed. With the improving sensitivity and resolution of radio telescope technology in the early 1970s, Vera Rubin and Kent Ford

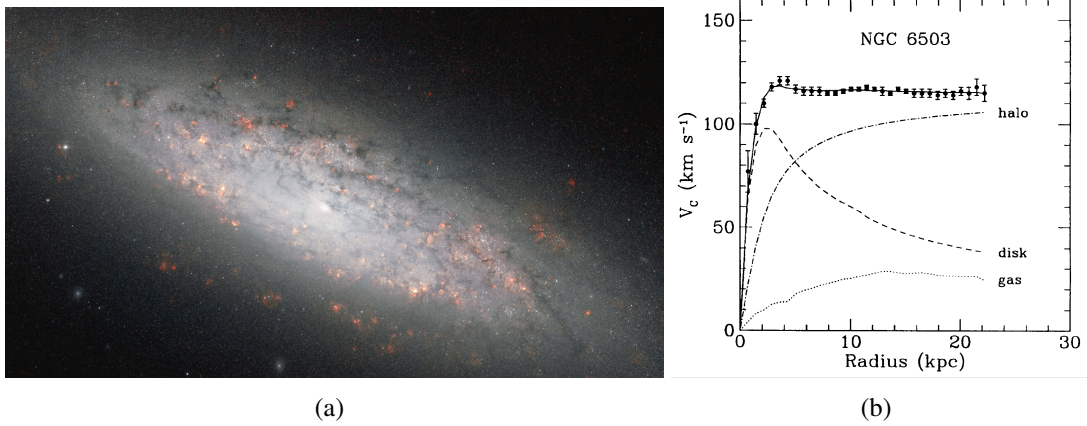


Figure 1: (a) The spiral galaxy NGC6503 [4]. (b) Measured rotation curve of NGC6503 with the function for the visible mass (dashed) and gas (dotted) content as well as the resulting dark matter halo (dash dotted) [5].

were able to measure the rotation velocity of interstellar hydrogen gas far beyond visible galactic discs [6]. They observed that the rotation velocity shows a flat distribution far outside these optically-visible boundaries. Figure 1 shows a picture of the spiral galaxy NGC6503 with the graph of its rotation curve. From Figure 1(b) it can be seen that the contribution of the luminous mass of the bulge disc of the galaxy (dashed line) together with the contribution from the interstellar gas (dotted line) cannot be added up to the mass content of the observed flat velocity distribution. Since the motion of stars is a result of their gravitational effect upon each other, this means that a new but unidentified type of matter contributes to the velocity distribution of the rotation curve, namely dark matter. It is therefore assumed that the luminous matter of a galaxy is embedded in a much bigger dark matter halo. The inferred contribution of such a dark matter halo surrounding the galaxy is also depicted in Figure 1(b) (dash dotted line).

2.1.2 Galaxy Clusters

The first indication for the existence of dark matter in the universe came from Fritz Zwicky when he studied the Coma galaxy cluster in 1933. A galaxy cluster is a structure with the typical size of a couple of megaparsecs in which several hundreds up to thousands of galaxies are bound together by gravity. Applying the virial theorem, which states that the magnitude of the total gravitation potential energy of a bound system is equal to twice the total kinetic energy, to the Coma galaxy cluster, he concluded that the mass of the cluster was much larger than the sum of the masses of the individual galaxies in the cluster.

Later it was discovered that large structures like galaxy clusters are not only optically visible but also emit strong X-ray radiation, originating from very hot gas between 10^7 to 10^8 K in the intergalactic space of the cluster. With satellites like the Chandra X-ray telescope the mass component of the galaxy cluster from the hot gas can be measured, since the X-ray emission is proportional to the plasma density squared. Nevertheless, the interstellar gas and the luminous galaxies do not sum up to the total amount of mass of the galaxy cluster.

Gravitational lensing gives an independent measure for the total mass of a cluster. It

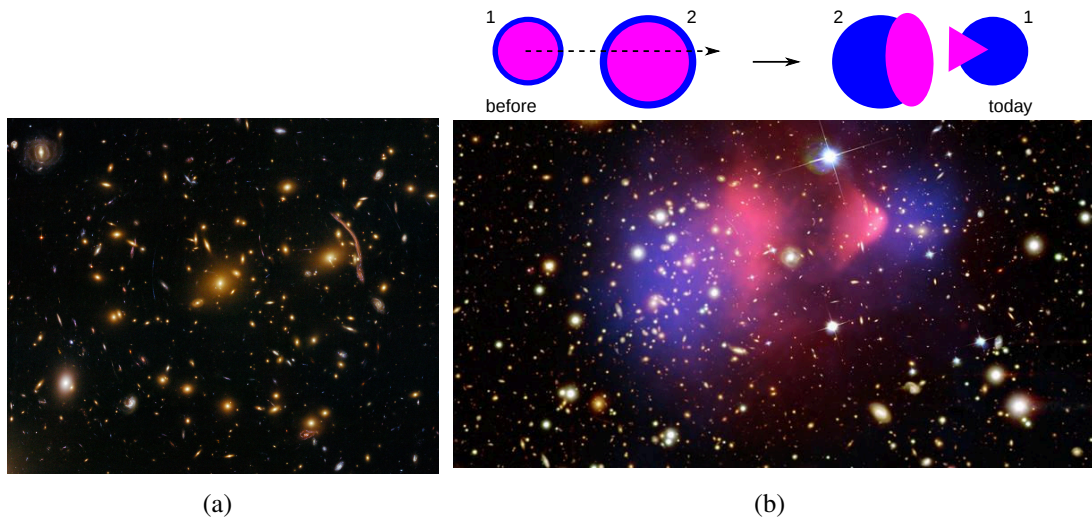


Figure 2: (a) The Abell 370 galaxy cluster, the first cluster where gravitational lensing was observed [7]. (b) The galaxy cluster 1E 0657-56, or bullet cluster, showing the hot, interstellar gas from X-ray spectroscopy (pink) and two dark matter contributions originating from two galaxy clusters [8] (blue), measured with gravitational lensing. The cartoon illustrates the passage of the two clusters through each other [9]. The collision is indicated by the merging interstellar gas, while the mass contribution from dark matter stays unaffected.

relies on Einstein's general theory of relativity and describes the effect that a massive foreground object, like a cluster of galaxies, bends light from a distant object behind it. This distorts the image of the background structure and sometimes creates multiple images of the same structure. The strength of this effect depends on the mass of the lens, and the distances between the observer, lens and background object. If these distances are known, the mass of the lens can be calculated. Figure 2(a) shows the Abell 370 galaxy cluster, acting as a gravitational lens. Many arcs and multiple images of distant galaxies are visible. Comparing the results from X-ray spectroscopy and gravitational lensing, it was found that the mass of the luminous galaxies and the interstellar gas do only make up $\sim 20\%$ of the total mass of the galaxy cluster [3]. The missing mass contribution to the total mass is inferred to come from dark matter.

The most striking evidence towards the existence of dark matter comes from the merging of two galaxies to form the *bullet cluster* 1E 0657-56 (Figure 2(b)). The hot baryon distribution (pink), resulting from interactions of the plasma of the two merging galaxy clusters, is measured by the Chandra X-ray telescope. It is clearly separated from the mass distribution obtained by gravitational lensing (blue). The separation comes from the merging of the two clusters. While the components of the hot gas interact with each other, the dark matter components pass collisionless through each other. The clear separation of the two dark matter components of the previously separated galaxy clusters is considered as evidence for the existence of dark matter.

2.1.3 The Cosmic Microwave Background

The most precise determination of the abundance of dark matter in the universe comes from the measurement of the cosmic microwave background (CMB). This electromagnetic radiation in the frequency range from 300 GHz to 300 MHz does not come from one specific source in the universe, but rather almost uniformly from every direction in the sky. The energy spectrum of the CMB is to a very good approximation a black-body spectrum with a peak frequency of 160.2 GHz which is in the range of microwave emission (Figure 3(a)). In general black-body spectra are formed when photons are continuously absorbed and re-emitted by matter. Since the universe today is mainly transparent to photons, the CMB must originate from the very early universe which was much hotter and denser than it is nowadays. According to the Big Bang theory the early universe consisted of a plasma containing all elementary particles that continuously interacted with each other. As the universe expanded, the previously uncoupled protons and electrons formed neutral atoms that could not absorb the photons anymore. At this point the universe became transparent to the photons and they decoupled from the interaction with the other particles, traveling through the universe since then. As the universe expands with time, the initial wavelength of the photons increases. This phenomenon is called redshift. According to Wien's displacement law, the peak wavelength of a black body spectrum is inversely proportional to the temperature. As a result the temperature of the of the CMB decreases with increasing photon wavelength. The black body spectrum of the CMB corresponds to a characteristic temperature of 2.72548 ± 0.00057 K, the current temperature of our universe [10].

Figure 3(b) displays an all-sky map of the cosmic microwave background measured by the Planck satellite. The CMB is found to be very smooth, only exhibiting very small anisotropies in the temperature at the level of 0.002 K. These incredibly small temperature fluctuations give insight into the composition of the early universe. The quantity that enables the comparison of the strength of the temperature fluctuation as a function of

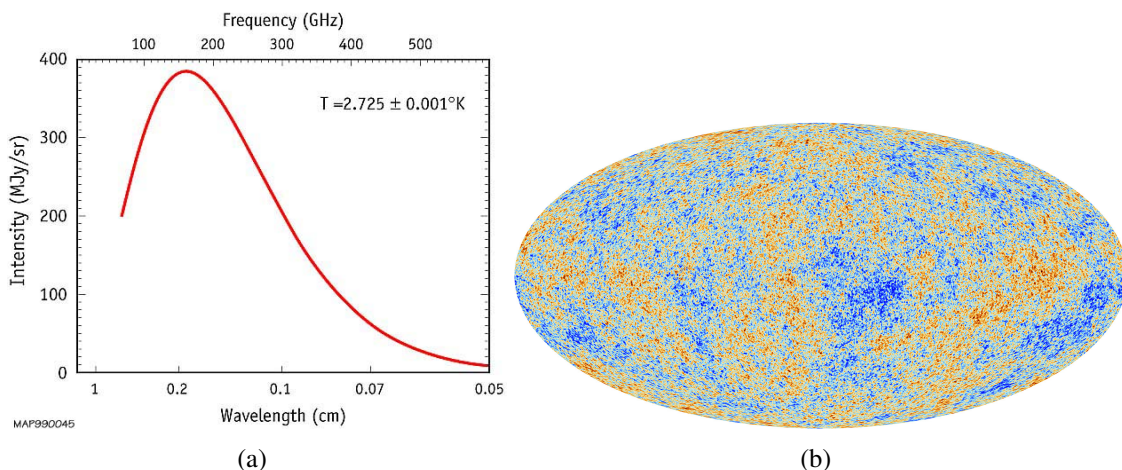


Figure 3: (a) The black body spectrum of the CMB measured by the FIRAS instrument on the COBE satellite. The error bars are a fraction of the line thickness [11]. (b) All-sky map of the CMB, measured with the Planck satellite. The different colours correspond to the temperature fluctuations [12].

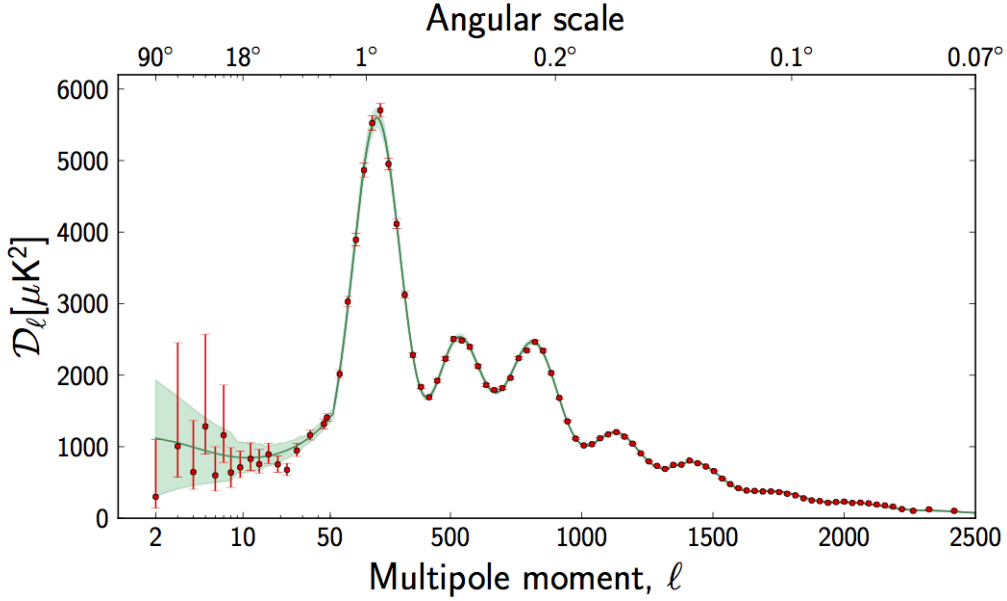


Figure 4: Temperature fluctuations of the CMB detected by Planck satellite in the angular power spectrum. The green curve is the fit of the data to the parameters of the standard model of cosmology and the pale green area around the curve shows variations of the standard model that best agree with the data [13].

the scale in the sky is called an *angular power spectrum*. Figure 4 shows the angular power spectrum derived from most recent Planck data. The quantity on the x-axis, the *multipole number* l , describes the difference between two directions in terms of their angular separation by $l = 180^\circ/\Theta$. Small values of l correspond to large scales on the sky. For any given value of l the value of the D_l on the y-axis denotes how much variation in the temperature is present in the CMB. The green curve shows the best fit of the six parameters of the standard model of cosmology to the data, the pale green area around the curve shows the predictions of all the variations of the standard model that best agree with the data.

Among the determined cosmological parameters are the physical baryon density $\Omega_b h^2$, the physical cold dark matter density $\Omega_c h^2$ and the dark energy density Ω_Λ . The physical baryon density $\Omega_b h^2$ consists of the critical baryon density Ω_b , the total density of matter needed for the universe to be spatially flat, multiplied by the square of the reduced Hubble constant h . Likewise for the physical dark matter density. The values that have been determined with data from the most recent measurements of the Planck satellite are displayed in Table 1. These parameters, including the dark matter density, represent the most precise numerical characterisation of the universe that is currently available.

Cosmological parameter	Value
$\Omega_b h^2$	0.02230 ± 0.00014
$\Omega_c h^2$	0.1188 ± 0.0010
Ω_Λ	0.6911 ± 0.0062

Table 1: Values of the physical baryon density $\Omega_b h^2$, the physical cold dark matter density $\Omega_c h^2$ and the dark energy density Ω_Λ from most recent planck results (2015) [14].

2.2 Dark matter candidates

There are countless models assigning different properties to their dark matter candidates. All these models have to fulfil several constraints that arises from the astrophysical observations and results of dark matter search experiments. Studies of the nucleosynthesis in the Big Bang set an upper bound on the abundance of baryonic matter in the universe, which can not account for the amount of dark matter that is found in the universe. Therefore, dark matter has to be a new, beyond the standard model type of matter. To account for the observed mass abundance in the universe and due to its main interaction mode through the gravitational force, dark matter is expected to be a massive and abundant particle. In addition, it can not interact electromagnetically, otherwise it would have been observed with telescopes. Further, it can only interact weakly with ordinary baryonic matter, since no interaction has ever been observed so far [3].

Non-relativistic or *cold* dark matter is currently the most compelling explanation for most cosmological observations. This type of dark matter is slow enough to allow mass clustering due to gravitation, which make it at present the biggest research are for dark matter. Among the large variety of models containing cold dark matter candidates, there exist two that were introduced to solve problems occurring in the Standard Model of particle physics without considering the dark matter problem in specific: the axion and the weakly interacting massive particle. These models give rise to particles that can explain the abundance of dark matter in the universe and therefore naturally solve the dark matter problem.

2.2.1 Axions

The axion is a pseudoscalar particle, associated with the solution of the strong CP problem in quantum chromodynamics that was proposed by Peccei and Quinn in 1977 [15]. The strong CP problem addresses the contradiction that even though quantum chromodynamics allows the violation of CP symmetry in strong interactions, it has never been observed experimentally. The mathematical description of CP violation is connected to the strong CP violating term Θ . This angle has been measured and is restricted by the large electric dipole moment to the extremely small value of $\Theta \leq 10^{-9}$ [16]. Thus, the strong CP problem can also be formulated as the question, why is Θ so close to zero? Peccei and Quinn suggested to promote Θ to a field by adding a new global symmetry. This symmetry is spontaneously broken which results into a new particle that fills in the role of Θ . This particle was called *axion* or pseudo-Nambo-Goldstone boson [17].

It is possible to model axion formation in the early universe via three mechanisms, that could provide for the missing dark matter in the universe today. Therefore, several experiments searching for axions as dark matter candidates exist. One of these experiments is called the Axion Dark Matter Experiment (ADMX). Using a resonant microwave cavity within a large superconducting magnet, the experiment aims to detect the very weak conversion of axion type dark matter into microwave photons. When the cavity's resonant frequency is tuned to the axion mass, interactions of nearby axions and the magnetic field of the detector is enhanced. This is expected to result in a small power deposit into the cavity of the order of a 10^{-24} W [18]. The group plans to take data with the second generation of ADMX in 2015 and expects to either discover dark matter axions or to rule out the dark matter axion theory completely [19].

2.2.2 WIMPs - Weakly Interacting Massive Particles

The leading particle dark matter candidates are *weakly interacting massive particles*, called WIMPs. They are predicted by several Standard Model extensions, for example the R-parity-conserving supersymmetry. A WIMP is characterised as a particle with a high mass between 10 GeV up to the TeV range, that only interacts via the weak nuclear force and gravity. Some WIMPs do not interact with ordinary matter via the electromagnetic force, they are therefore “invisible“ to electromagnetic measurements.

According to standard cosmology, WIMPs were in thermal and chemical equilibrium with the Standard Model particles after inflation. This means that WIMPs were produced from and annihilated into Standard Model particles at equal rates. Due to the expansion of the universe, the temperature dropped at some point under the mass of the WIMPS and the reaction rate became smaller than the Hubble expansion rate of the universe. WIMPs were not produced anymore and did not annihilate back to Standard Model particles. The WIMP density thus remained essentially constant from this point onwards. The process where the WIMPs drop out of thermal equilibrium is referred to as *freeze-out* of dark matter [20]. The present WIMP relic density in terms of self-annihilation cross section $\langle \sigma v \rangle$ is approximately given by

$$\Omega_c h^2 \sim \frac{3 \cdot 10^{-27} \text{ cm}^3 \text{ s}^{-1}}{\langle \sigma v \rangle}, \quad (2)$$

with σ as the thermal average of the total annihilation cross section of the WIMPs with velocity v . To agree with the measured value of the cold dark matter density from Planck data (Chapter 2.1.3), the self-annihilation cross section $\langle \sigma v \rangle$ is required to be of the order of $10^{-26} \text{ cm}^3/\text{s}$. The order of this cross section is typical for weak interactions in the Standard Model, which justifies the name WIMPs [21]. The local WIMP density in our solar system is estimated to be $\rho_0 = 0.3 \pm 0.1 \text{ GeV}/\text{cm}^3$ [22].

There are three different types of WIMP detection mechanisms (Figure 5). One detection mechanism is the production of dark matter at particle colliders like CERN. If dark matter was created, it would escape without interacting with detector material, but carrying away a noticeable amount of energy and momentum. From the missing energy, the existence of dark matter could be inferred. Indirect detection techniques work with the

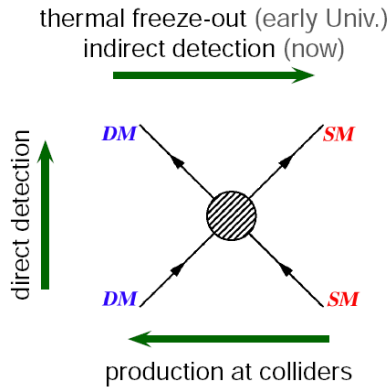


Figure 5: Dark matter detection principles depending on the dark matter production or annihilation channel. The three possible mechanisms are dark matter production, direct and indirect dark matter detection [23].

observation of WIMPs through their annihilation or decay far away from earth, for example at the galactic centre. These experiments are typically telescopes, aiming to measure an excess of gamma rays at certain regions of the sky, since gamma rays are the expected self-annihilation products of WIMPs. One of these experiments is the Fermi Large Area Telescope [24]. Direct detection experiments aim to observe the effects of WIMP-nucleus collisions as the WIMP passes through a detector situated at earth. Currently, the most competitive direct detection experiments are the XENON100 and the LUX experiment. Both use dual-phase xenon time projection chambers to search for dark matter.

2.3 Direct dark matter detection

From the following section onwards, the focus will lie on dark matter in terms of WIMPs. This type of dark matter almost exclusively interacts via the weak force and gravity with ordinary matter and is therefore expected to be abundant in our galaxy. Consequently, several highly sensitive terrestrial detectors are currently aiming to detect WIMPs.

2.3.1 Detection principles

WIMPs primarily interact with the atomic nucleus. Since they are non-relativistic, this interaction takes the form of elastic scattering with an energy transfer of up to tens of keV. The differential rate, that is the interaction rate in terms of the recoil energy E_r , is given by the following equation in its most general form:

$$\frac{dR}{dE_r} = \frac{\rho_0}{m_N m_\chi} \int_{v_{min}}^{\infty} v f(v) \frac{d\sigma_{WN}}{dE_r}(v, E_r) dv, \quad (3)$$

where ρ_0 is the local WIMP density, m_N and m_χ the target and the WIMP mass respectively, $\frac{d\sigma_{WN}}{dE_r}(v, E_r)$ is the differential cross-section for the WIMP-nucleus elastic scattering and $f(v)$ the WIMP velocity distribution in the detector frame [25]. It describes the number of expected WIMP-nucleus interactions per kg detector material per day per unit deposited energy. Figure 6 shows the differential recoil spectrum for the different target materials xenon, argon and germanium assuming fixed WIMP mass of 100 GeV and the differential recoil spectrum for 10 GeV WIMPs in xenon. For a fixed target mass at low recoil energies, the differential rate decreases more rapidly with increasing recoil energy for lighter WIMPs. At low recoil energies and a fixed WIMP mass, the highest differential rate is achieved with the heaviest target material xenon. The consistency of a measured energy spectrum within experiments with different target nuclei would confirm a WIMP scattering.

By scattering off ordinary matter, WIMPs deposit energy in the corresponding material. Energy deposit in matter can evoke electronic excitation (ionisation), phonons (heat transfer) and scintillation photons (Figure 7). The type of energy deposit depends on the target material. Therefore, deploying different detection channels requires different detection techniques. For example the DCMS-II experiment deploys germanium crystals to detect dark matter interactions via the ionisation and the phonon channel whereas the XENON collaboration uses the property of liquid xenon to respond to incoming radiation with the emission of scintillation light and ionisation. In order to detect these types of signals, the XENON collaboration deploys dual-phase xenon time projection chambers. An elaborate list of different detector principles can be found in [27].

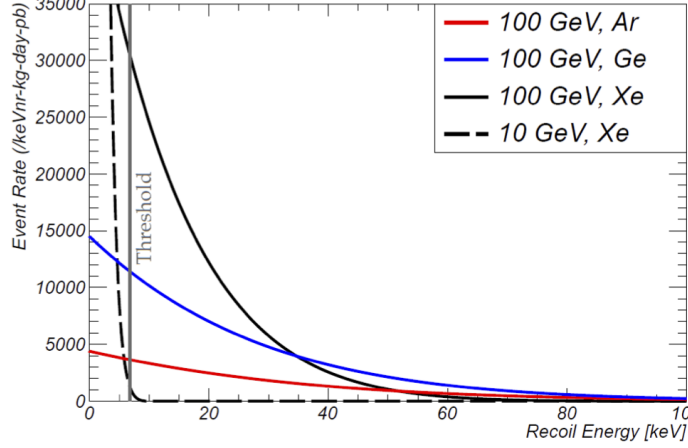


Figure 6: Differential WIMP-nucleon recoil spectrum with different target nuclei assuming a WIMP mass of $m_\chi = 100\text{GeV}$ and $m_\chi = 10\text{GeV}$ [26]. For a fixed target mass the differential recoil spectrum decreases steeper for a lighter WIMP mass. For a fixed WIMP mass at low recoil energies, the differential event rate is higher for higher target masses.

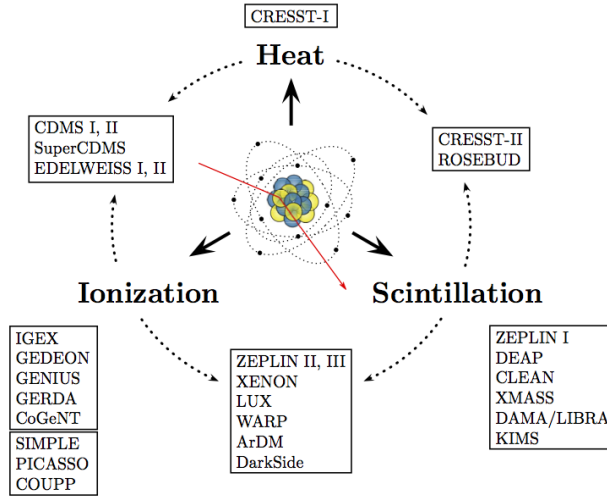
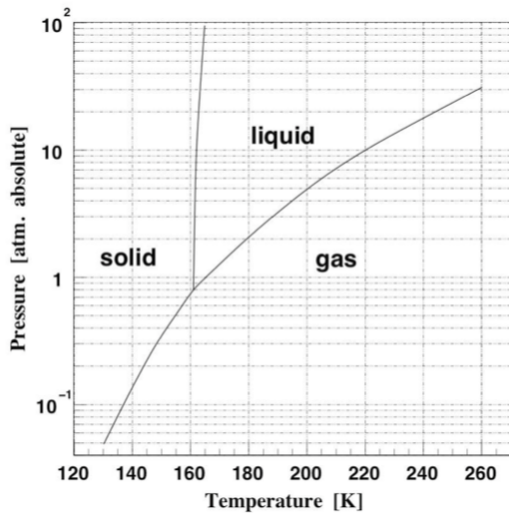


Figure 7: Different excitation channels of energy deposit in matter and dark matter detection experiments ordered according to the excitation channels used in the experiments [27].

2.3.2 Xenon as detector material

In their liquid form, noble gases are excellent media to build large, homogeneous and self-shielding detectors to search for WIMPs. From all noble gases, only argon and xenon are currently used as target materials for dark matter search. Both materials emit scintillation light and are ionised when energy is deposited. Argon offers a high pulse shape discrimination power, but with an intrinsic radioactivity of 1 Bq/kg from β decays [28], it is a less favoured detector material for low background searches.

With a mean atomic weight of 131.3, xenon is the heaviest noble gas. It does not have any long-lived radioisotopes except ^{127}Xe with a half-life time of 36.3 d, which means that xenon essentially does not have any intrinsic radioactivity. It has nine stable isotopes



(a)

Xenon property	Value
Atomic number, Z	54
Mean atomic weight	131.29
Melting point, (1 atm)	161.39K
Boiling point, (1 atm)	165.05 K
Gas density, (273 K, 1atm)	5.8971 g/L ²
Liquid density (165.05 K, 1atm)	3.057 gcm ³
Relative permittivity (gas), ϵ_r	1.00
Relative permittivity (liquid), ϵ_r	1.96
Scintillation wavelength	178 nm

(b)

Figure 8: (a) Phase diagram of xenon and (b) selected properties of xenon. For a more elaborate table the reader is referred to [29].

that allow for a spin dependent and spin independent dark matter search [28]. Figure 8(a) shows the phase diagram of xenon. At atmospheric pressure, xenon has a relatively high boiling point point at 165.05 K. Considering that liquid noble gas detectors are operated at a slightly higher pressure at the order of 3 bar, xenon as detector medium allows modest cryogenic systems for gas liquefaction. At the boiling point, xenon has a density of 2.94 g/cm³. Due to this high density, the stopping power is high enough that background radiation deposits energy in the first centimeters of the outer layer of the detector medium. This is called *self-shielding*. Furthermore, in liquid xenon the energy of the emitted scintillation photons is smaller than the absorption energy, which makes xenon transparent to its own scintillation light. The scintillation light spectrum of xenon has its peak at 178 nm with a width of 14 nm, which is in the vacuum ultraviolet (VUV) range. The electrons from the ionisation signal in liquid xenon have a high mobility, which allows to separate them from the xenon ions with an external field [27]. Figure 8(b) summarizes the most important xenon properties.

An incoming particle interacts with the liquid xenon either via electronic or nuclear recoil. In general electronic recoils are caused by muons, γ and β radiation, while nuclear recoils are caused by neutrons and WIMPs. A recoiling particle in liquid xenon creates a track of excited xenon atoms and electron-ion pairs. The excited xenon atoms and the xenon ions form excited molecular states, by colliding with neighbouring xenon atoms. These excited molecular states, called *excimers*, subsequently relax into the ground state and thereby emit scintillation light:



The excimers consist of a combination of singlet and triplet states. The singlet state has a lifetime of 4.3 ns and the triplet state a lifetime of 22 ns [30]. The fraction of these states differs for electronic or nuclear recoil interactions, resulting in different pulse shapes of the scintillation light. This property gives the possibility to discriminate between background events and possible dark matter interactions. Due to the very small

difference in the duration of the lifetime, the study of the pulse shape for low energy interactions is still ongoing.

2.3.3 Dual-phase xenon time projection chambers

Dual-phase xenon time projection chambers make use of large, homogenous volumes of xenon in liquid and gaseous form to measure the scintillation and the ionisation signal of an energy deposit. These detectors are often called time projection chambers (TPC), due to their ability to determine the 3D position of the interaction point like traditional gas TPCs.

Figure 9(a) depicts a dual-phase xenon time projection chamber, with liquid (LXe) and gaseous xenon (GXe) as detector material. On both ends, the detector is equipped with arrays of photomultiplier tubes (PMTs) to measure the scintillation and the ionisation signal. The prompt scintillation light, called *S1 signal*, arrives immediately at the PMTs. By applying an electric drift field E_d along the z -axis of the detector, the electrons from the ionisation are separated from the ionised xenon atoms. They drift towards the liquid-to-gas interface, where they are extracted from the liquid xenon into the gas phase by an electric extraction field E_g . In the gas phase, the electrons emit scintillation light due to electroluminescence. The emitted light is detected by the PMTs as *S2 signal*. The number of the photons emitted in gas is proportional to the number of electrons produced in the ionisation signal. Since the electrons drift with a finite speed along the TPC, the S1 and

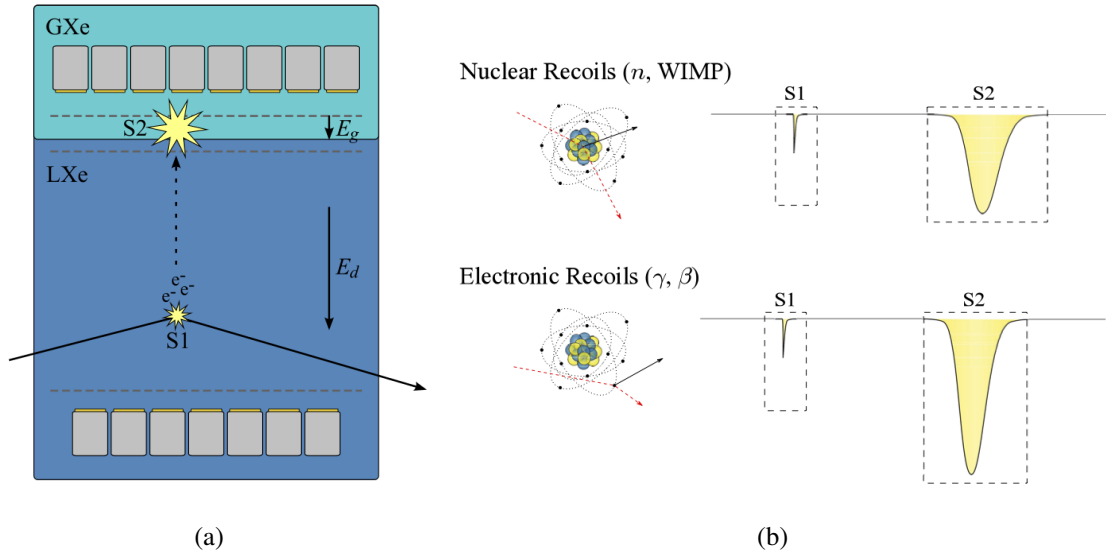


Figure 9: (a) Working principle of xenon dual-phase time projection chamber. The interaction of particles with the liquid xenon results in the emission of scintillation light (S1 signal) and ionisation of xenon atoms. The electrons from the ionisation are drifted upwards with an electric field. With a stronger field, they are extracted in the gas phase where they emit the S2 signal. The S2 hit pattern in the PMT arrays and the time difference between the S1 and the S2 signal allows the position reconstruction of the interaction point. (b) Sketch of nuclear (top) and electronic recoils (bottom) and the corresponding S1 and S2 signals. The shapes of the S1 and the S2 signal differ for different interaction types [31].

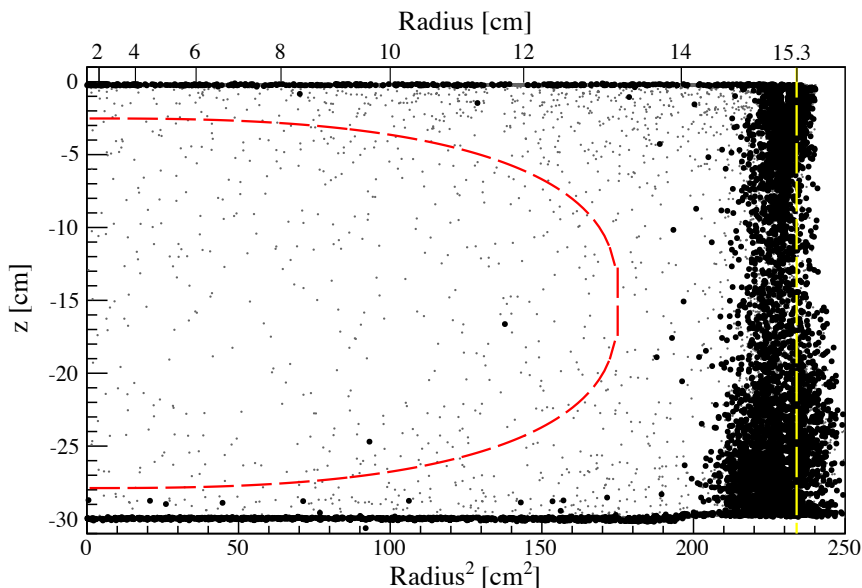


Figure 10: Distribution of nuclear recoil (black dots) and electronic recoils (grey dots) in a 225-live day science run of XENON100. The red dashed line indicates the fiducial volume. Most of the interactions occur in the passive xenon shield, while only two nuclear recoil events fall inside the fiducial volume. This is consistent with the background expectation of 1.0 ± 0.2 events [32].

the S2 signal arrive at different times. The time delay between the arrival of the S1 and the S2 signal is called *drift time*.

For a fixed drift- and extraction field, the shape of the signals differs for electronic and nuclear recoils (Figure 9(b)). For the S2 signal, this is because the ionisation density in liquid xenon is much higher for tracks from a nuclear than for an electronic recoil [27]. Thus, for electronic recoil interactions, the electrons can be more efficiently separated from the xenon ions, which results in a larger S2 signal. The S1 signal also differs for electronic and nuclear recoils, but due to the small difference of the life time of the singlet and triplet state, the study of the S1 pulse shape is still ongoing.

To discriminate between electronic and nuclear recoils, and therefore between background events and dark matter candidate events, the XENON collaboration deploys the ratio $\log_{10}(S2/S1)$. It is larger for electron recoils than for nuclear recoils. An additional technique for posterior background reduction is the position reconstruction of the interaction point. The hit pattern of the S2 signal in the top PMT array gives information about the position of the event in the xy -plane and the time difference between S1 and S2 signal allows to determine the z coordinate of the interaction. The longer the drift time, the closer to the bottom PMT array the interaction occurred. The 3D localisation allows for background reduction in the data, since most background interactions occur in the outer layers of the target volume. A fiducial volume, which consists of a inner central area of the TPC, is defined in the detector material, the rest of the liquid xenon is considered as passive shield (Figure 10). Nuclear recoil events occurring inside the fiducial volume are possible dark matter candidates.

3 The XAMS setup

XAMS, an acronym for Xenon AMsterdam, is the Netherlands first dual-phase xenon time projection chamber that is built and tested at the Nikhef institute in Amsterdam. Nikhef is actively involved in the construction of the XENON100 and the XENON1T experiments and the Dark Matter group at Nikhef develops the XENON1T event builder, processing software and works on the XENON100 data analysis. The design of the XENON100 experiment and its successor XENON1T relies on findings of small scale dual-phase xenon time projection chambers like XAMS. Demonstrators like XAMS continuously contribute to the enhancement of the measurement devices, the improvement of readout electronics and software as well as the improvement of the data analysis techniques and are therefore indispensable for the success of the XENON experiment.

Figure 11 shows a picture of the XAMS setup, indicating the five parts it can be divided into. The main part in the centre of the setup is the detector vessel, containing the TPC (green). On the left side the gas system (red) can be seen. It consists of two storage bottles for the xenon, two recuperation dewars, a recirculation pump, a getter for purification and the gas flow control board. The cryogenic system of the detector is indicated in blue. It is made up of a heat exchanger and the cooling tower. The monitor and control tower with the slow control is indicated in orange. In purple, on the right side of the setup, is the data acquisition (DAQ) computer.

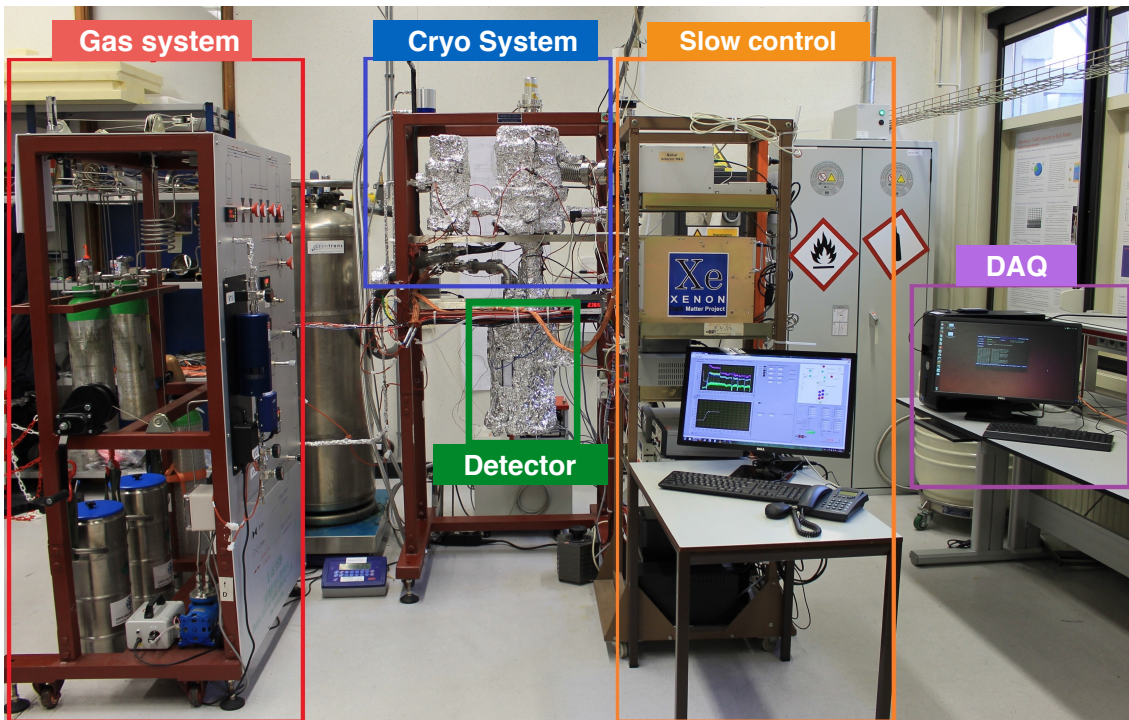


Figure 11: The XAMS facility. The detector vessel is at the centre of the setup, the gas system on the left, above the detector vessel is the cryogenic system and on the right are the DAQ and slow control tower.

3.1 The dual-phase xenon time projection chamber

The following chapter gives an overview over the core of the XAMS setup: the dual-phase xenon time projection chamber.

3.1.1 Teflon structure and electric fields of the time projection chamber

The XAMS time projection chamber consist of 16 cylindrically shaped PTFE rings (Figure 12(a)). PTFE, or Teflon, is a commonly used material in xenon TPC structures for several reasons. First of all, PTFE is a very good electrical insulator, which makes it a very suitable material for operations with high voltages like the ones applied in xenon TPCs. For the voltages applied at XAMS, the breakdown voltage of PTFE is more than 30 times stronger than the highest applied field along the TPC [33]. Second, the dielectric constant of Teflon¹ only deviates by 7.1 % from the dielectric constant of liquid xenon². This minimises the distortion of the electric field applied along the TPC. Finally, PTFE has a high reflectivity of about 47 % to 66 % for light in the VUV region, the region in which xenon emits scintillation photons [36]. This means that PTFE as a holding structure significantly improves the detection efficiency of scintillation photons emitted in liquid xenon in the TPC.

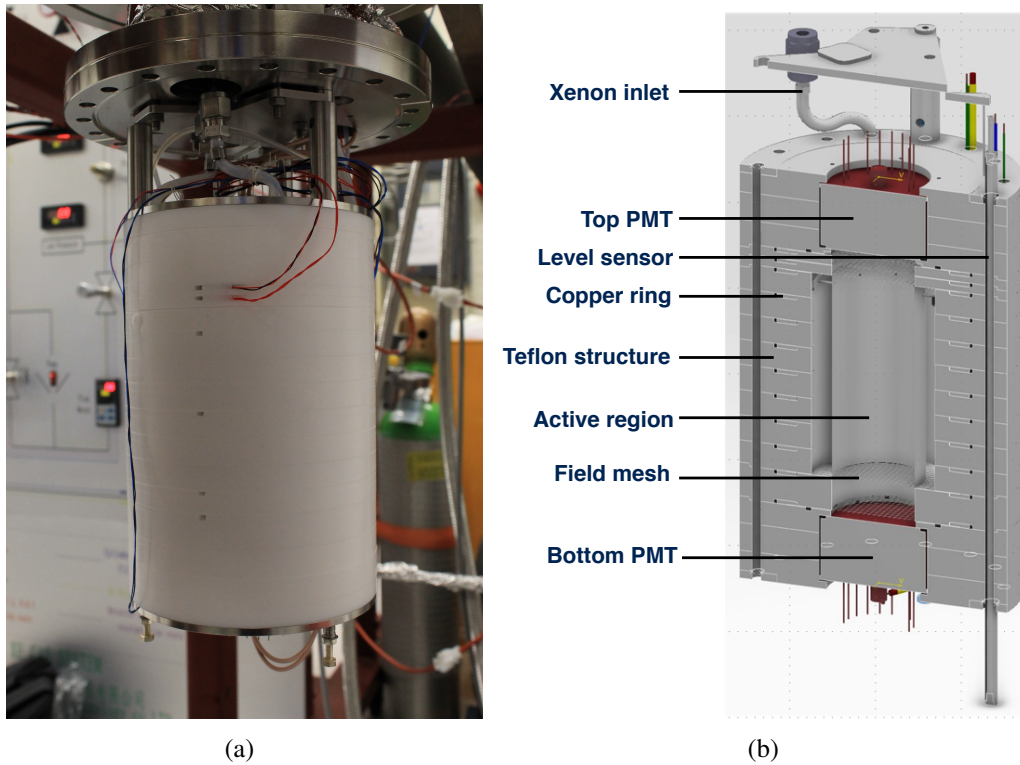


Figure 12: (a) The Teflon structure of the XAMS TPC with two Pt100 temperature sensors. (b) 3D cross section through the XAMS time projection chamber, indicating the different elements of the TPC (image credit: Rob Walet)

¹ $\epsilon_{\text{Teflon}} = 2.1$ [34]

² $\epsilon_{\text{LXe}} = 1.96$ [35]

Embedded in the Teflon structure are a xenon inlet and outlet for filling and recirculation, two PMTs, a level and six temperature sensors, field meshes, field shaping copper rings and the active detector region (see Figure 12(b)). The PTFE slices allow the variation of the drift length of the TPC. The full Teflon structure measures 20.9 cm in z-direction at room temperature and shrinks by about 2 mm when cooled down to $-90\text{ }^{\circ}\text{C}$. To keep the TPC at level, three steel springs are constantly pushing the structure upwards towards the top flange of the vessel that contains the TPC. For optimal light reflection, a hollow PTFE cylinder is inserted in the active region. The active volume, that is the region from which the S1 and S2 events originate, measures 10.0 cm in z-direction and has a diameter of 4.4 cm at cryogenic temperatures (Figure 13(a)). This translates to 0.434 g of liquid xenon. During operation the detector is filled with 5.2 kg of xenon, which means that 8.4 % of the filled xenon is inside the active volume.

Five $150\text{ }\mu\text{m}$ thick stainless steel meshes create the drift and amplification field of the TPC and seven equidistant copper rings ensure the homogeneity of the electric field (Figure 13(b)). The field meshes are (from bottom to top) the bottom screening mesh, the cathode, the gate mesh, the anode and the top screening mesh. Between the cathode and the gate mesh is the *drift field*. It separates the electrons from the ionisation interaction from the xenon ions and drifts the electrons upwards towards the gate mesh. During operation with xenon gas, the applied drift field is 0.10 kV cm^{-1} , while with liquid xenon the applied drift field is 0.60 kV cm^{-1} . The stronger drift field in liquid xenon ensures a

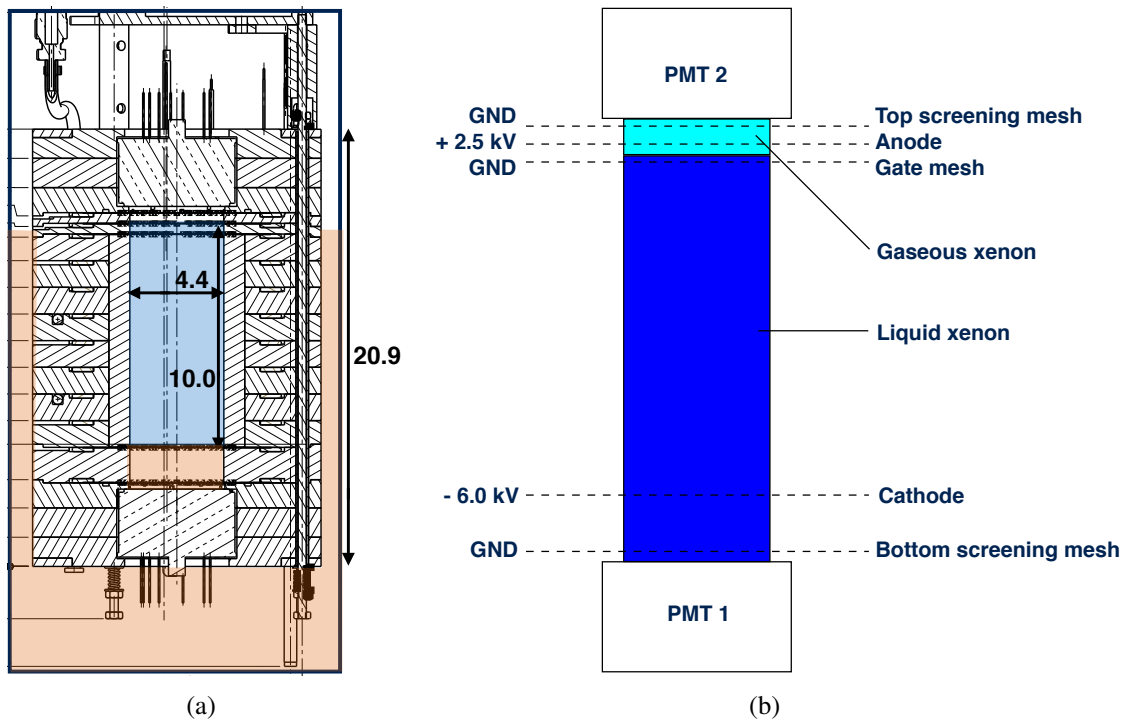


Figure 13: (a) Cross section through the TPC indicating the active liquid xenon region (blue) and the inactive liquid xenon region (orange). The active volume of XAMS contains 0.434 kg of liquid xenon. The dimensions are in cm. (b) Schematic cross section through the XAMS TPC, indicating the field meshes and their voltages during liquid operation (Image credit: Rolf Schön).

higher separation efficiency of the electrons from the ionised xenon atoms. Between gate mesh and anode is the *extraction - or amplification field*. The applied field of 5 kV cm^{-1} extracts the electrons out of the liquid xenon and accelerates them towards the anode. In the gas phase the electrons emit the S2 scintillation light that is detected by the PMTs. The top and the bottom screening mesh are kept at ground in order to shield the PMTs from the high voltages applied at the cathode and anode.

3.1.2 Scintillation light detection with photomultiplier tubes

At XAMS the scintillation light is detected with two photomultiplier tubes (PMTs) at the top and at the bottom of the TPC. A PMT is a photosensitive vacuum tube that consists of an entrance window, a photo cathode, electron multipliers (dynodes) and an anode (Figure 14(a)). When a photon enters the photocathode, the bialkali material of the photocathode emits electrons into the vacuum due to the photoelectric effect. The electrons are directed towards the dynodes, where they are multiplied by the process of secondary electron emission. The multiplied electrons are collected at the anode to produce the output signal. PMTs are usually sensitive down to single photoelectrons.

XAMS is equipped with two Hamamatsu R6041-406 photomultiplier tubes (see Figure 14(b)). There are several properties that characterise the strength of the output signal of a PMT. The most important properties, that determine the choice of the PMT type, are the quantum efficiency and the gain of the PMT. The quantum efficiency is the ratio of photoelectrons emitted from the photocathode to the number of incident photons at the photocathode and it depends on the wavelength of the incoming photons. The wavelength of the emitted scintillation light in liquid xenon is 178 nm. For this wavelength, the Hamamatsu R6041-406 PMTs have the highest quantum efficiency with 30 % (Figure 15(a)). The gain, or the current amplification, is the ratio of the number of electrons measured at the anode to the number of photoelectrons emitted by the photocathode and depends on the number of dynodes inside the amplification region. The gain of the Hamamatsu PMTs

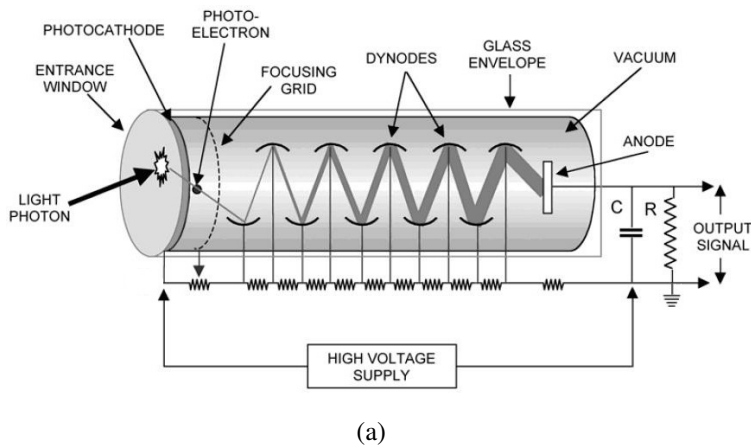
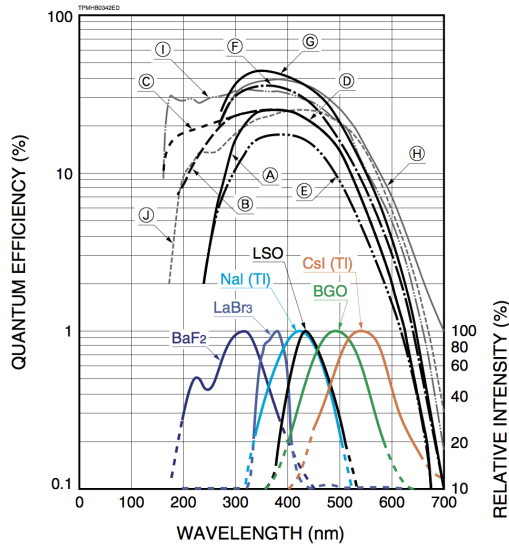


Figure 14: (a) Working scheme of a typical PMT. Incoming photons emit electrons into the vacuum of the tube when entering the photocathode. The multiplied electrons produce an output signal at the anode [37]. (b) Hamamatsu R6041-406 photomultiplier tube used at XAMS. Image taken from [38].



(a)

Property	Value
Photocathode diameter	50 mm
Number of dynodes	12
Suggested operating voltage	800 V
Maximum operating voltage	1000 V
Gain (at 800 V)	10^6
Minimum operating temperature	-110°C
Spectral range	160 nm to 650 nm
Quantum efficiency	30% (at 178 nm)
Rise time	2.3 ns
Transit time	16 ns
Transit time spread	0.75 ns

(b)

Figure 15: (a) Typical photocathode quantum efficiency and emission spectrum of scintillators. The low temperature bi-alkali photocathodes are indicated with the letters *I* (down to -110°C) and *J* (down to -186°C). Photocathode *I*, which is implemented in the XAMS PMTs, has with 30% the highest quantum efficiency at 178 nm [39]. (b) Specifications of the Hamamatsu R6041-406 photomultiplier tubes used at the XAMS setup [39].

for an applied voltage of -800 V is 4.0×10^6 at room temperatures. A detailed overview of the calibration of the XAMS PMTs can be found in [38].

Figure 15(b) summarises further specifications of the Hamamatsu R6041-406 PMTs. The transit time is the time interval from the arrival of the light pulse at the photocathode to the moment the output at the anode reaches its maximum and the transit time spread is the fluctuation in transit time between individual pulses. The PMTs used at XAMS have a transit time of 16 ns, and a spread of 0.75 ns. The rise time, the time it takes the output current to raise from 10 % to 90 %, is 2.3 ns [39].

3.1.3 The determination of the liquid level in the TPC during operation

To have full knowledge of the existing conditions inside the TPC, it is crucial to determine the level of the liquid xenon inside the detector volume. In dual-phase xenon time projection chambers this is usually done with a capacitive sensor, referred to as level meter. A capacitance sensor is a capacitor that exploits the property that materials in the liquid and gaseous phase have different dielectric constants. A level meter that is to some extent filled with a liquid and with a gas can be interpreted as two separate capacitors with different dielectric constants connected in parallel. The height of the liquid level in a cylindrical capacitance sensor, like the one deployed at XAMS, is determined by:

$$C(h) = \frac{2\pi\epsilon_0\epsilon_g l}{\ln\left(\frac{R_b}{R_a}\right)} + \frac{2\pi\epsilon_0(\epsilon_l - \epsilon_g)h}{\ln\left(\frac{R_b}{R_a}\right)} \quad (5)$$

$$\Rightarrow h(C) = \frac{\ln\left(\frac{R_b}{R_a}\right)C - 2\pi\epsilon_0\epsilon_g l}{2\pi\epsilon_0(\epsilon_l - \epsilon_g)}, \quad (6)$$

where ϵ_0 , ϵ_g and ϵ_l are the vacuum permittivity, the gaseous and the liquid dielectric constant of the corresponding material, R_b the inner radius of the outer capacitor rod, R_a the outer radius of the inner capacitor rod, l the total length of both capacitors and h the height of the liquid level inside the capacitance sensor.

The level meter used at XAMS is 85 mm long, with a 30 mm long slit along the z-axis to avoid capillary effects and for xenon inlet (Figure 16). This rather short design was chosen after the previous, 275 mm long level meter was not operational due to internal stresses. The reduced length does not affect the informative value of the level meter in the crucial area between the gate and the anode mesh. In this area of 5 mm distance, the gas-to-liquid interface has to be measured and controlled. The level meter extends from 13.4 mm below to 71.5 mm above the gate mesh. Using Equation 5, the inner radius $R_b = 4.0$ mm, the outer radius $R_a = 3.0$ mm and a difference in the dielectric constant of liquid and gaseous xenon of $\epsilon_l - \epsilon_g = 0.87$ the expected capacitance of the level meter in liquid xenon is 0.17 pF mm^{-1} .

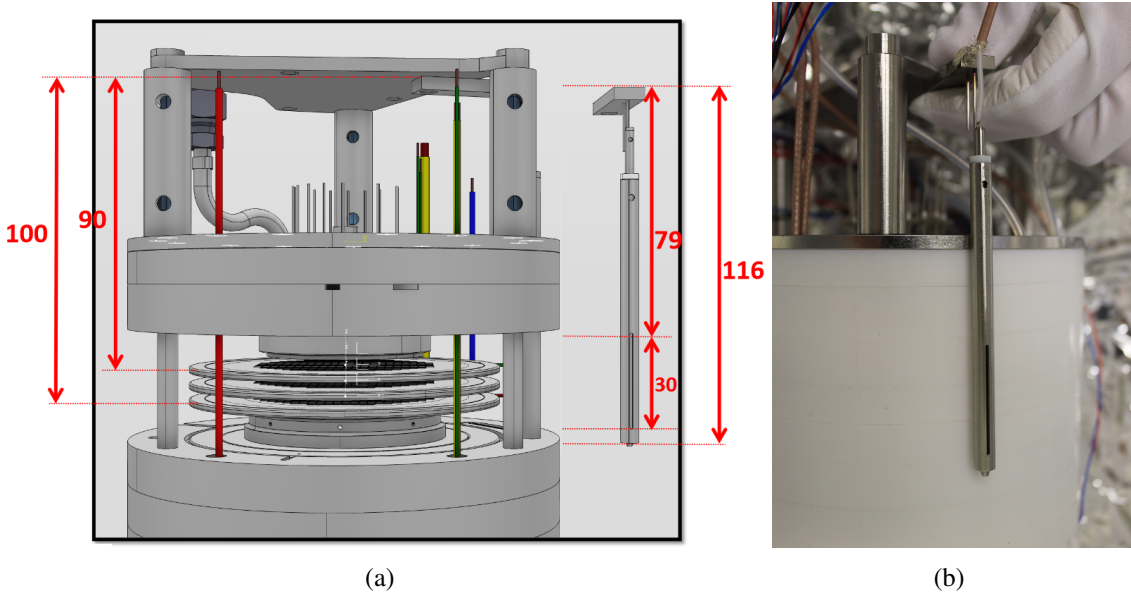


Figure 16: (a) Scheme of level meter next to gate mesh, anode and top screening mesh, showing that it covers the amplification area. Dimensions are in millimeter. Image credit: Rob Walet. (b) Level meter next to the Teflon structure of the TPC. It extends down to 13.4 mm below the gate mesh.

The capacitance of the level meter at XAMS is read out with an Arduino board, a microcontroller board with integrated development environment based on the Processing programming language. The board is programmed to constantly charge and discharge the capacitor. While charging the capacitor it reads out up to 50 voltages along the charging curve of the capacitor. It depends on the capacity C of the fully charged capacitor at a voltage V_0 , which is charged through a resistor with resistance R :

$$V(t) = V_0(1 - e^{-\frac{t}{RC}}). \quad (7)$$

For each measured voltage $V(t)$, the capacitance C is calculated, averaged and displayed in the slow control framework. The fluctuation in the capacitance readout corresponds to 0.02 pF. For more information on the level meter readout, see [40].

The level meter is calibrated in two steps. It is first calibrated and tested outside the TPC in liquid nitrogen and second, inside the TPC for operation in liquid xenon. To calibrate the level meter in liquid nitrogen it is attached to a stainless steel mounting platform that is placed inside a dewar. The dewar is filled with liquid nitrogen until the level meter is completely covered. While the liquid nitrogen evaporates the capacitance as well as the height of the liquid nitrogen is monitored. The liquid nitrogen calibration curve is displayed in Figure 17(b). The error on the capacitance readout corresponds to 0.02 pF and the error in the height of the level ranges from 0.5 cm, if the level is closer to the eye of the observer, and increases to 1 cm as the level decreases further. Within the detection range of the level meter, that is between 0 cm and 8.5 cm, the capacitance depends linearly on the height of the liquid level. The data points outside the range of the level meter, display a constant capacitance as they correspond to an completely empty and completely full level meter. A linear fit to the detection region of the level meter gives a capacitance of $0.0819 \pm 0.0004 \text{ pF mm}^{-1}$. This deviates by 1.3% from the expected value, calculated with Equation 5 to 0.083 pF mm^{-1} . That the measured value deviates from the expected value is due to the influence of the anti-capillary slit, that is not taken into account in Equation 5.

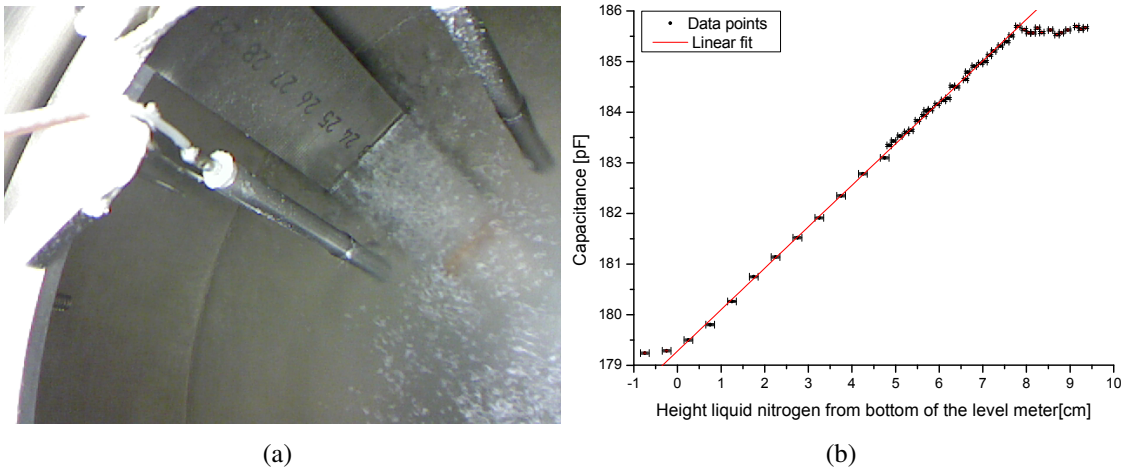


Figure 17: (a) Picture of the calibration setup, with the level meter immersed in liquid nitrogen (left). The capacitance from the level meter and the height of the level are stored for calibration. (b) The resulting calibration curve with a proportionality factor of $0.0819 \pm 0.0004 \text{ pF mm}^{-1}$.

The calibration of the level meter in liquid xenon aims to correlate the capacitance read out with the height of the liquid xenon level in the detector. Initially, three Pt100 sensors inside the setup were intended to give three calibration points along the level meter. Pt100 sensors are resistance thermometers, that measure the resistance of a small ceramic bracket depending on the surrounding temperature. A temperature drop can be observed when the initially in gas positioned sensors are suddenly immersed in the rising liquid xenon. During operation, these sensors showed inconsistent results. A more useful tool for the calibration of the level meter in situ has been proven to be data acquisition during the filling of the amplification area with liquid xenon. This calibration method will be elaborated in this chapter, a detailed overview of data acquisition at XAMS is given in Chapter 3.5.

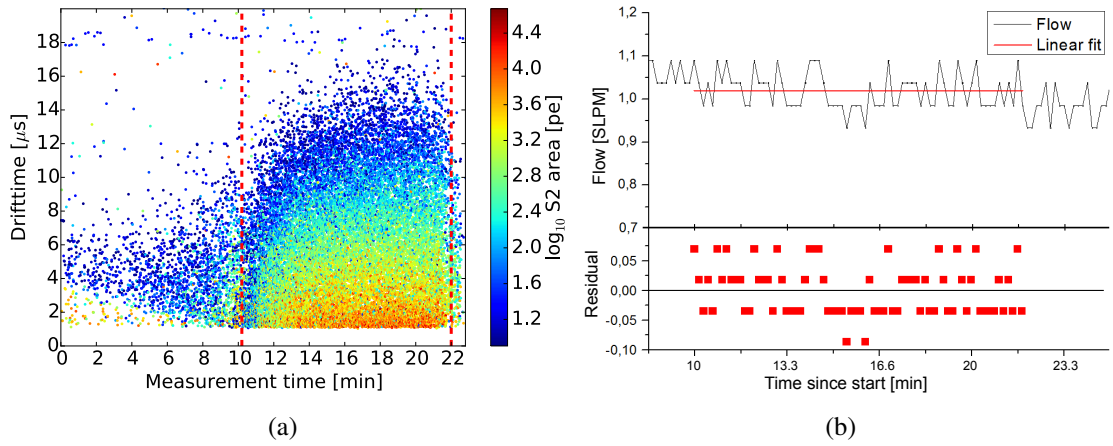


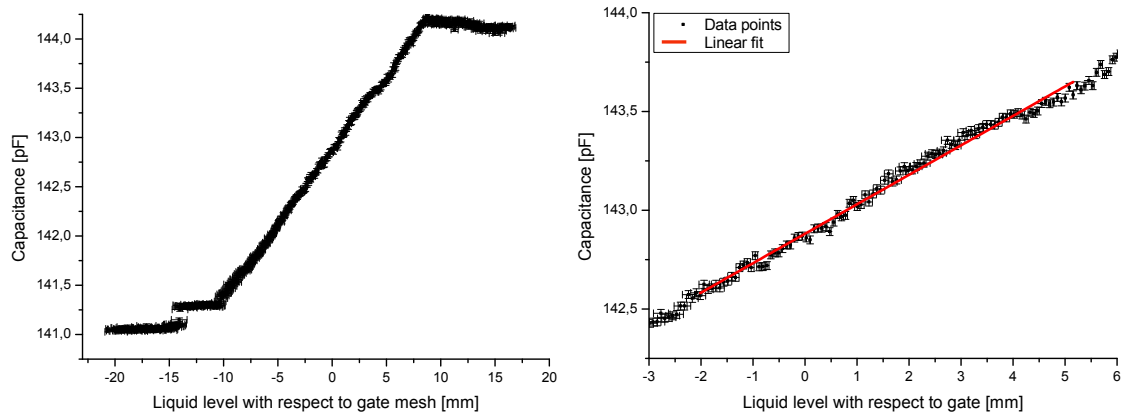
Figure 18: (a) Drift time during increasing liquid level. The time stamps at the dashed line indicate the gate mesh at $t_g = 10.4 \pm 0.6$ min and the anode $t_a = 21.5 \pm 0.6$ min. (b) The xenon flow during the filling of the region between gate mesh and anode. The even distribution of the residual of the fit allow the conclusion that the flow is constant at 1.019 ± 0.05 SLPM.

During the filling of the amplification region with liquid xenon, continuous data of natural background radiation, like radon decays and cosmic rays, has been taken at a rate of 250 Hz. In Figure 18(a) the corresponding drift time depending on the time since the start of the measurement is displayed. Every measurement point in Figure 18(a) corresponds to an event with at least one S1 and one S2 signal. When the liquid level passes the gate mesh at $t_g = 10.4 \pm 0.6$ min, the amplification field extracts electrons from the liquid. As a result the number of S2 signals drastically increases. As the liquid level passes the anode at $t_a = 21.5 \pm 0.6$ min, the electron extraction stops almost immediately. As a result, the number of S2 signals drops.

These two time stamps can be used to calibrate the level meter. Figure 18(b) shows, that the xenon flow F during the filling of the level meter can be assumed to be constant at 1.019 ± 0.05 SLPM. The liquid level L is then proportional to the integrated flow F , with a proportionality constant α :

$$L = \alpha \int_{t_g}^t F dt \quad (8)$$

As calibration point t_g , t_a and the known distance between the gate mesh and the anode of 5.02 mm at -90 °C are used. The proportionality constant is derived to be $\alpha = 0.444 \pm 0.021 \frac{\text{mm}}{\text{SL}}$. The entire calibration curve of the level meter during filling is displayed in Figure 19(a). The more the height of the liquid level differs from the calibration points, the bigger is the error on the height of the level. The fit of the calibration curve in the crucial measurement area between gate and anode is displayed in Figure 19(b). The fit gives that the capacitance per unit filling length is $0.1491 \pm 0.0015 \text{ pF mm}^{-1}$. This deviates from the expected value $0.1688 \text{ pF mm}^{-1}$ (Equation 5) by 12 %. This is due to the effect of the anti-capillary effect that is not taken into account in the calculations. The smallest measurable distance of the level meter is 0.12 mm, which corresponds to the readout fluctuation of 0.02 pF



(a) Capacitance readout depending on the height of the liquid level (b) Calibration between gate mesh and anode

Figure 19: (a) Capacitance readout depending on the height of the liquid level of the full level meter in liquid xenon. (b) Calibration curve between the gate mesh and anode. The proportionality is found to be $0.1491 \pm 0.0015 \text{ pF mm}^{-1}$.

3.2 Xenon gas recirculation and purification system

The scintillation detector material in the dual-phase time projection chamber of XAMS is liquid and gaseous xenon. The xenon has to be as pure as possible to avoid losses of scintillation light and ionisation electrons. Electronegative impurities like oxygen are the main absorbents of drift electrons [41] while water is the main absorbent of scintillation light [42]. To purify the xenon, it is kept in a closed cycle trough which, before and during operation, it is constantly pumped and purified.

Figure 20 shows the schematics of the XAMS purification circuit in a piping and instrumentation diagram. The system is divided into a high pressure region and a low pressure region, which are separated by a pressure regulator between PT101 and PT102. The high pressure region is tested up to 88 bar and is found near the three storage cylinders A, B and C. Cylinder C was used to fill the xenon into the circulation setup, while the cylinders A and B are used for storing of and refilling with xenon. There is a total of 10 kg of xenon available for XAMS. The low pressure region is connected to the detector volume. Its pressure is limited to 3.7 bar by a burst disc. Besides being a basic safety requirement, this protects the system from overpressurisation and therefore destroying the sensitive measurement devices in the detector.

The recirculation and purification of the xenon is conducted in the low pressure region of the gas system. The recirculation is done with an EMP MX-808ST-S double-membrane pump (PM101). It pumps liquid xenon from the detector vessel to the gas system. On its way, the liquid xenon passes a heat exchanger where it is evaporated. In the gas system it passes through a hot getter (SAES MonoTorr PS3-MT3-R-1, see Figure 21(a)) (GT101). The getter contains a powder of an alloy of zirconium, vanadium and iron, that absorbs the electronegative impurities in the xenon gas. The output temperature of the xenon gas passing through the getter is $< 50 \text{ }^\circ\text{C}$. After the filling of the detector it was observed, that xenon passing through the getter is even purified when the getter is switched off, that is when the getter material is not heated up to $350 \text{ }^\circ\text{C}$. Figure 21(b) shows the duration of the measurement in hours depending on the drift time of the electrons, while the xenon

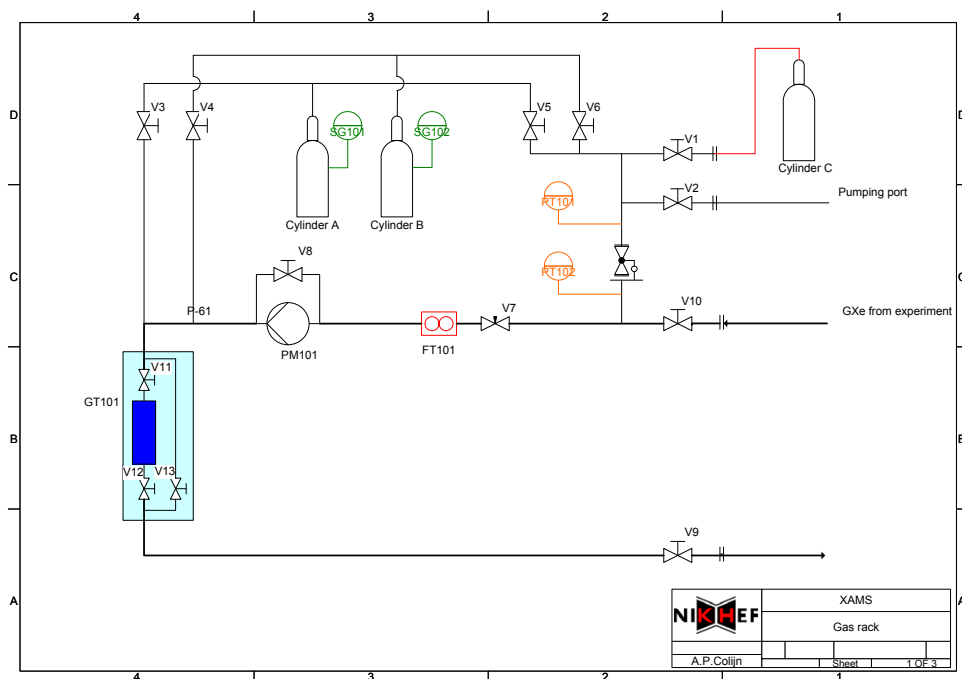
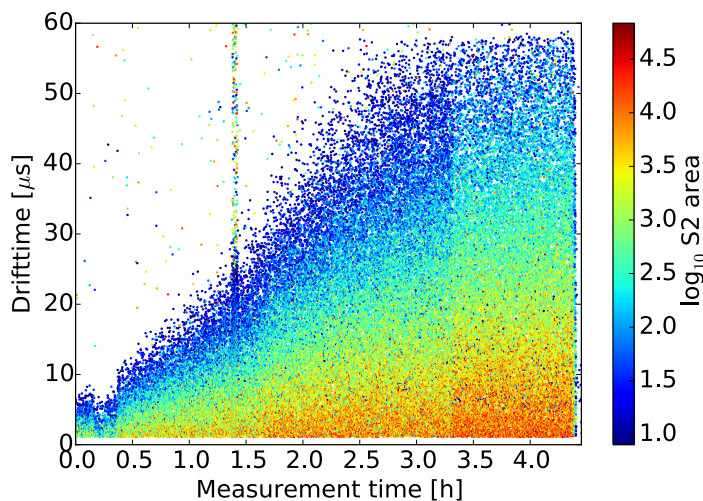


Figure 20: XAMS piping and instrumentation diagram. It is divided into a high (C, D) and a low pressure region (A, B, C). The high pressure region contains the xenon storage bottles and is tested up to 88 bar. The low pressure region contains the recirculation pump and the getter for purification. It is limited to 3.7 bar and connected to the detector vessel.



(a)



(b)

Figure 21: (a) The MonoTorr getter at XAMS. (b) Increasing drift time with the duration of the measurement proves the purification of xenon in the switched off getter. The break down of the curve below 0.5 h corresponds to an automatic shutdown of the cathode after a spark, the increased event rate at 1.5 h is due to a Cs source that was shortly placed next to the detector, at 1.7 h the getter was switched on and the jump at 3.3 h corresponds to a decrease in the liquid level.

passes through the getter. It can be seen that as time passes, the drift time of the electrons increases until the maximum drift time of 58 μs is reached, which means that the amount of impurities in the xenon decreases. The color coding displays the S2 area. With purer xenon the S2 area is expected to grow, coloring the measurement points in red.

The maximum flow the getter can operate with is 5 standard liters per minute (SLPM). This corresponds to a maximum of 42 kg of xenon circulated per day. Nevertheless, during normal operation the flow is of the order of 2 SLPM which corresponds to a circulation of 16.8 kg per day. When filled, the detector contains 5.2 kg (1000 SL) of xenon, therefore all xenon passes through the getter about three times per day. The gas leaving the getter has an impurity level of less than 1 ppb. The flow of the xenon gas through the getter is regulated by a needle valve (FT101).

3.3 Liquifying xenon in the cooling tower

After passing through the getter in the gas system, the xenon gas enters the cryogenic system. To liquefy the xenon gas at a pressure of 2.5 bar it needs to be cooled down to $-90\text{ }^\circ\text{C}$ (Figure 8(a)). The cryogenic system consists of three elements: the heat exchanger, the cooling tower and the detector vessel. To decrease the heat transfer to the inner volume, the whole cryostat is surrounded by an insulation vacuum between double walls of stainless steel. The insulation vacuum is kept at a vacuum below 10^{-6} mbar with a turbo molecular pump. In the heat exchanger, incoming hot xenon gas from the getter is cooled down by the outgoing cold liquid xenon, that is pumped to the gas system. Thereby 90% of the incoming xenon gas is already cooled down to the boiling point and liquefied.

When it enters the cooling tower, it condenses at the cold finger. The condensed xenon forms droplets, which fall through a funnel into a pipe leading to the detector volume. At the beginning of the cooling process the detector vessel is still at ambient temperatures, which causes the xenon droplets to evaporate and thereby cool down the detector volume. Once it reaches a constant, low temperature, the droplets falling in the detector start filling it up with liquid xenon.

A cross section of the cooling tower is displayed in Figure 22. The cooling tower receives its cooling power from a pulse tube refrigerator (PTR). To provide cooling power the PTR constantly compresses and decompresses helium gas adiabatically. By this the cold head, a copper block inside the insulation volume, is constantly cooled down. The cold head is in direct thermal contact with the cold finger, a copper block inside the cryogenic system. With two PT100 sensors the temperature of the cold finger can be monitored. A heating element is placed between the cold finger and the coupling block. The cooling temperature is regulated by varying the power of the heating element with a proportional-integral-derivative controller (PID controller). During operation the cold finger is kept at a temperature of $-90\text{ }^\circ\text{C}$.

In case of a power failure in the lab, the PTR can not provide cooling of the liquid xenon anymore. A failure of the cooling power causes the liquid xenon in the detector to heat up and expand, resulting in an increase of the pressure inside the detector. To avoid overpressurisation, the inner volume is equipped with coils for emergency cooling with liquid nitrogen. If the pressure in the detector exceeds a configurable pressure of 2.7 bar, a solenoid valve opens the connection to a pressurized dewar filled with liquid nitrogen.

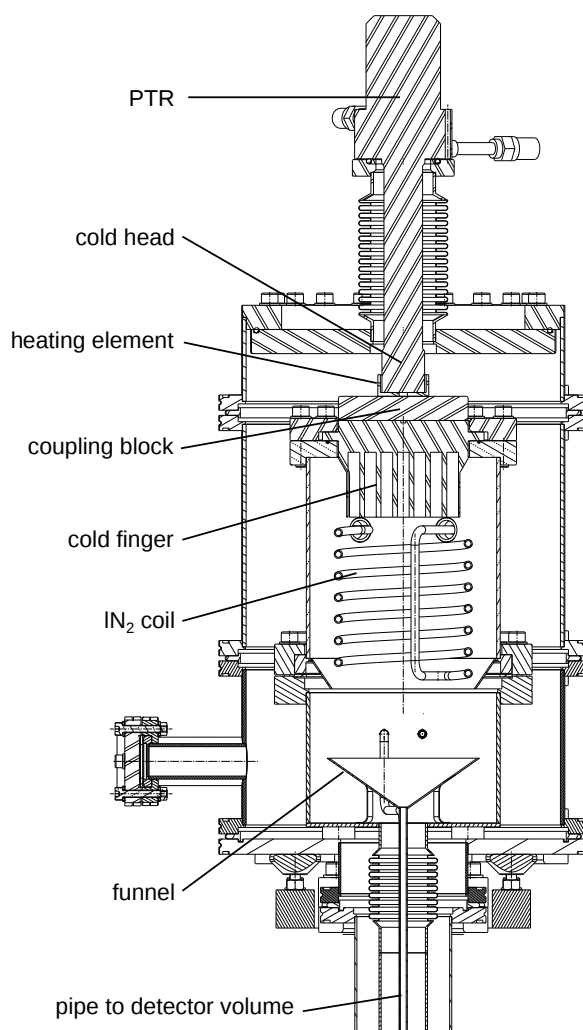


Figure 22: The XAMS cooling tower. A pulse tube refrigerator provides cooling power to the cold head. A copper block transmits heat from the cold finger inside the detector volume. Incoming, cold xenon gas condenses at the cold finger and forms droplets, that fall into the detector vessel through a funnel. The temperature inside the detector is controlled by a heating element, which is connected to a PID controller [9].

Liquid nitrogen flows through the coil until the pressure in the detector drops to 2.5 bar, when the solenoid valve closes again to avoid freezing of xenon around the liquid nitrogen coil. If the pressure crosses the upper threshold again, the valve opens to allow again the nitrogen cooling. With the constantly opening and closing solenoid valve, the emergency cooling from a full liquid nitrogen dewar lasts for 27 hours.

3.4 Monitoring the system: The detector slow control

The detector slow control is a Labview programme, that monitors and logs detector parameters and allows to set control parameters. The monitor parameters give an overview over the conditions inside the detector. They are namely the temperatures inside and outside the detector vessel, measured with 22 Pt100 temperature sensors, the pressure in the

high and low pressure section at the gas board, the pressure in the detector vessel, the flow as well as the integrated flow of the xenon gas through the detector. Furthermore, the capacitance from the level meter is read out, which allows to determine the height of the liquid level in the detector (Figure 23). The slow control allows to set the temperature setpoint at the cold head, which controls the temperature inside the detector volume and therefore the liquefaction of xenon.

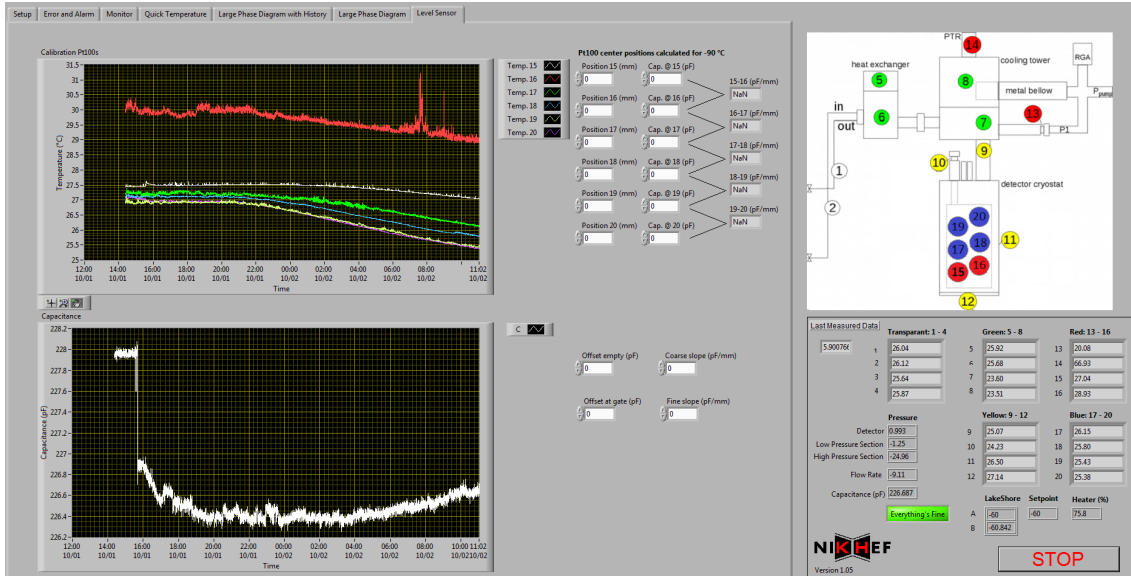


Figure 23: The slow control framework of XAMS with the monitor of six temperature sensors inside the TPC (top) and the level meter capacitance (bottom) during operation with liquid xenon. An overview over all Pt100 sensors, the pressure and the xenon flow is on the right.

Furthermore, the emergency alarm system for the case of a power failure in the lab is connected to the slow control PC. During a power failure the PC is powered by a UPS battery, which lasts for 45 minutes. The UPS also keeps the solenoid valve and the pressure gauge operational. Under alarm conditions, that is when the pressure in the detector rises above a configurable threshold or when the PC is powered via the UPS, the emergency alarm system of XAMS sends out text messages and emails to emergency staff. In case of an alarm, the emergency staff has to recuperate the xenon in the XAMS detector immediately. For this reason, all group members of the Dark Matter group at Nikhef obtained a safety training and a training in emergency recuperation.

3.5 The data acquisition and processing at XAMS

XAMS runs with the most up to date readout and data processing software that is developed for the XENON1T experiment. Therefore, XAMS is actively contributing to the processing software for XENON1T, which is developed in the Dark Matter group at Nikhef. Figure 24 shows a scheme of the data acquisition (DAQ) chain at XAMS.

The analog signal coming from the PMTs is converted to a digital signal with the V1730 CAEN digitizer. The digitizer readout is monitored and controlled with the XENON1T readout software *Kodiak* that runs on the DAQ PC. With an optical link connection, the

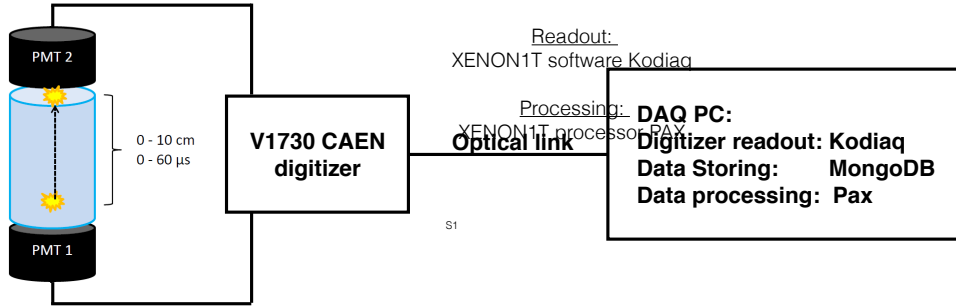


Figure 24: Data acquisition chain at XAMS. The signal from the PMTs is read out with the V1730 CAEN digitizer. Via an optical link it is transferred to the DAQ PC where it is stored and processed.

digitized signal is transferred to the DAQ PC where it is stored in a *MongoDB* database. Further processing is conducted by the XENON1T data processing software *pax*.

3.5.1 The V1730 CAEN digitizer and XENON1T readout software Kodiaq

Data acquisition at XAMS is carried out with the V1730 CAEN digitizer that houses one analog-to-digital converter chip (ADC) per channel (Figure 25(a)). An ADC is a device that converts a continuous, physical signal, like a voltage, into a digital number that corresponds to the amplitude of the signal. In general an ADC performs the conversion from analog to digital periodically. Therefore the sampling rate and the energy resolution of an ADC is of great importance. The V1730 CAEN digitizer is a Flash ADC waveform digitizer with 8 channels. It has a resolution of 14 bits and a sampling rate of 500 MS/s



(a)

```

xams@xams-Vostro-410: ~/kodiaq/kodiaq/src/slave
kodiaq - Data Acquisition Software Standalone Mode
Status: RUNNING Rate: 273 Hz @ 85.3063 MB/s
Buffer: 327656 bytes
file: ./DAQConfig.ini
Output: MongoDB: localhost:run5.measurement_008
Messages:
2015-03-20T13:59:23 - Started kodiaq
2015-03-20T14:01:08 - Reading file DAQConfig.ini
2015-03-20T14:01:08 - Initializing electronics
2015-03-20T14:01:10 - Start of run
Options: (p) stop run (q)
uit

```

(b)

Figure 25: (a) The V1730 CAEN digitizer [43]. (b) The graphical user interface of Kodiaq. It displays the configuration file, the data storage location and run information like start- and stop time of the run as well as trigger and data rate.

Property	Value
Dimensions	1-unit wide VME 6U module
Channels	8
Resolution	14 bits
Max. dynamic range	$2 V_{pp}$
Sampling rate per channel	500 MS/s
Sampling speed	2 ns per sample

Table 2: Specifications of the V1730 CAEN digitizer for the PMT readout [43].

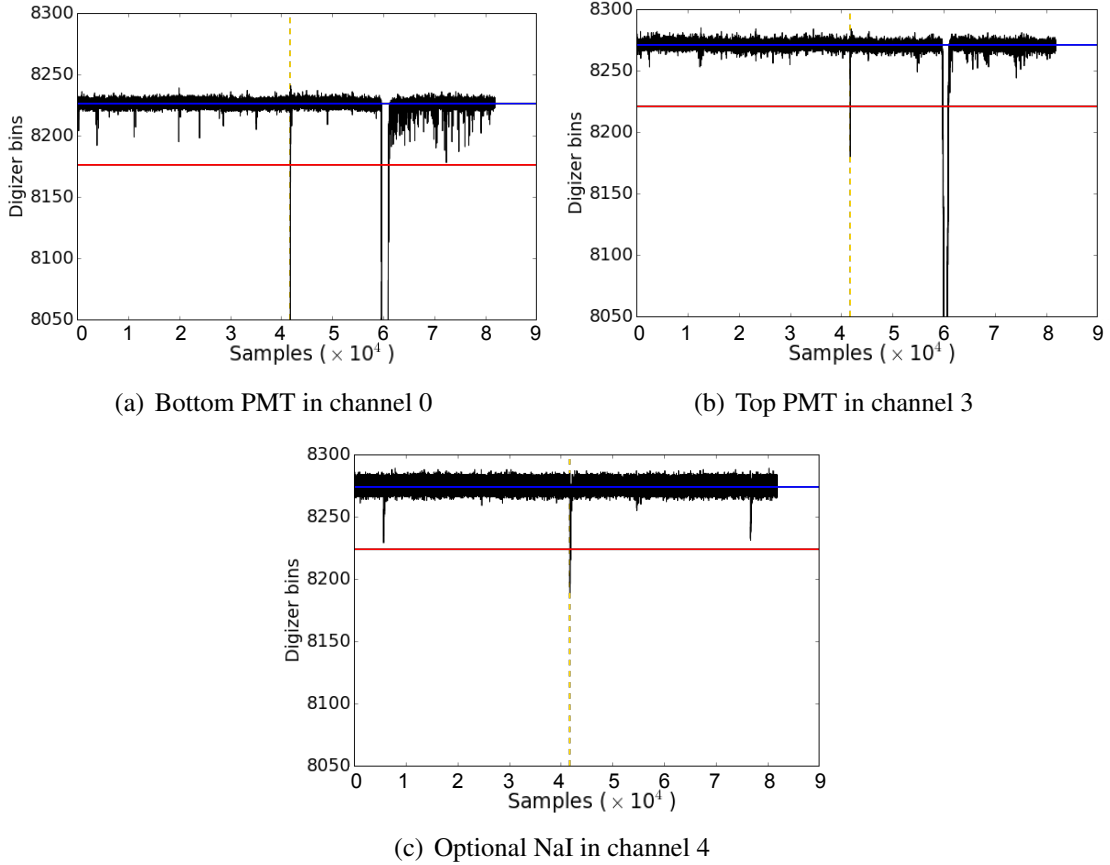


Figure 26: Trigger settings in the different digitizer channels during data acquisition. The bottom PMT is connected to channel 0 (Figure (a)), the top PMT to channel 3 (Figure (b)) and an optional NaI crystal for external trigger on γ -rays is connected to channel 4 (Figure (c)). The baseline (blue) is calculated from the first 100 samples, the trigger threshold for each channel (red) is at 50 (6 mV) bins below the baseline in order to trigger on the S1 signal and not on noise occurrences. The dashed yellow line indicates event on which the trigger occurred. As the waveform drops below the trigger threshold coincidentally in all deployed digitizer channels, the waveforms from each channel are transferred to the DAQ PC.

per channel. The high resolution and the fast sampling frequency make the digitizer well suited for liquid scintillator systems coupled to PMTs like the XAMS setup [43]. Further properties of the V1730 CAEN digitizer are listed in Table 2.

The digitizer is controlled from the DAQ PC with the standalone version of the XENON1T readout software Kodiaq. Figure 25(b) shows the graphical user interface of Kodiaq. The software loads options from a configuration file onto the digitizer, starts the data acquisition, manages the storage of the data in MongoDB and stops the acquisition. The options in the configuration file determine the acquisition mode of the digitizer. The file contains information about the trigger type, the trigger threshold, the time window of the stored information before and after the trigger occurrence and the dynamic input range.

During operation, data acquisition is triggered on a coincidence signal between the bottom PMT in channel 0 and the top PMT in channel 3 (Figure 26). In addition, there is the option to trigger externally on γ -rays with a NaI crystal in channel 4. The trigger threshold in each channel is set to 6 mV below the baseline. This means that data acquisition is triggered on the S1 signal. The baseline varies for different digitizer channels and it was observed that the digitizer needs to run for 10 minutes until the baseline of each channel stabilises. If a waveform drops below the trigger threshold coincidentally in all connected channels, the waveform of each channel is transferred to the DAQ PC. The time window of one event during a run in liquid xenon is set to 160 μ s, due to a maximum drift time of about 60 μ s. With a sampling speed of 2 ns per sample, this corresponds to about 80 000 samples per event window. To ensure that the S1 and the S2 signal are recorded, the trigger signal is set to the middle of the event window by choosing the post trigger window to be half of the event window. To capture the amplitude of the S1 signal, which is about 1 V, the dynamic input range of the digitizer is set to 2 V_{pp} with the baseline in the center of the window. The transferrable data rate of the digitizer is limited to 80 MB/s by the optical link. The raw data obtained from the digitizer is stored in a MongoDB 3.0.0 database in binary form. Within MongoDB the data from the measurements is stored in *collections*, which are grouped into different *databases*.

3.5.2 Data processing and analysis

Kodiaq automatically stores the raw waveforms from the digitizer in a MongoDB database. The raw waveforms are processed by the XENON1T processing software pax (processor for analyzing xenon). The processing software outputs an *avro*-file and an *hdf5*-file. The *avro*-file contains the compressed, raw waveform data. This format allows simple storage of the original data and supports reprocessing. The *hdf5*-file holds the output of the cluster and peak finding algorithm of the processor. If a signal inside a PMT passes a 7σ threshold above the baseline, it is classified as *hit*. To cluster the hits to *peaks*, pax compares the gapsize between two hits in both PMT channels. If the gap size is bigger than 1 μ s, a new peak is defined. All peaks of both PMT channels are summed up to form the *sum waveform*. Then the classification algorithm classifies the peaks as S1, S2 or unknown signal, depending on the width and the amount of photo electrons contributing to the peak. Finally, relevant peak properties like peak type, height, position, width and area are calculated and stored in the *hdf5*-file. For a limited data rate of 1 Hz, pax allows to process data online, that means data processing parallel to data acquisition. This is especially useful during the filling of the detector. During normal operation the data rate can reach up to 250 Hz, which means that the data can only be processed once the measurement is completed.

Pax offers the option to display the processed event. Figure 27 shows such a typical

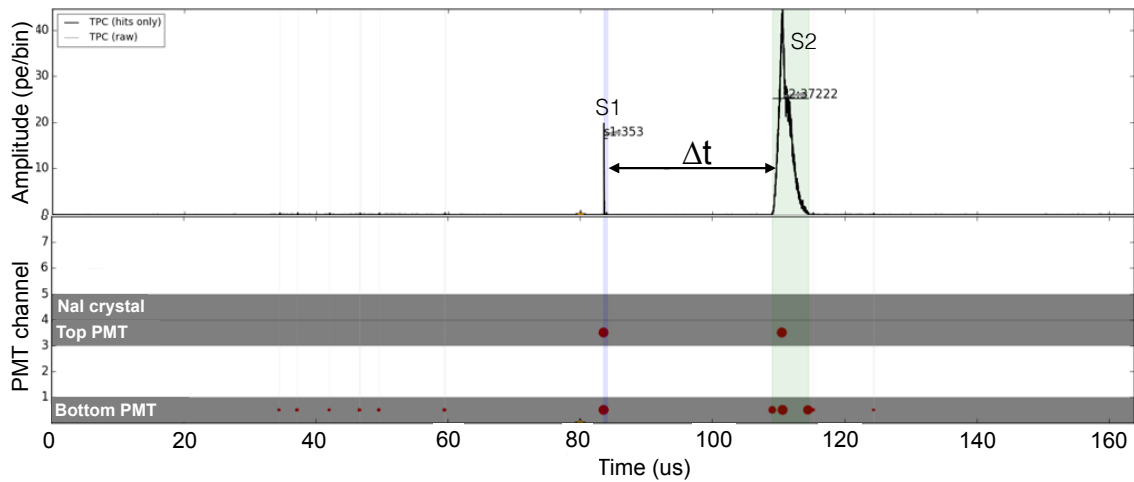


Figure 27: Pax output of the sum waveform with S1 and S2 classifications of a typical 511 keV event in liquid xenon (top) and the display in which PMT channels the hits occurred (bottom). In this measurement the two PMTs in the TPC and an external NaI crystal were connected to the digitizer.

pax output of an S1 and S2 signal from a 511 keV γ -ray in liquid xenon, injected at the center of the TPC. The top plot shows the sum waveform of the event with the classification and the number photoelectrons that corresponds to the area of the signal. The green band indicates an S2 signal, the purple band a S1 signal. The width of the bands show the time spread that is taken into account for the classification of the signal. The bottom plot shows the maximum of the hits in the different PMT channels, namely in channel 0 for the top PMT, channel 3 for the bottom PMT and channel 4 for an external NaI crystal. A performance test of the data acquisition chain with a waveform generator is performed in [44].

4 Collimator setup for the electronic recoil calibration of XAMS

For the electronic recoil calibration of the XAMS TPC, two radioactive sources are deployed: a 191.2 kBq ^{137}Cs and a 370 kBq ^{22}Na source. The ^{22}Na source can be combined with a collimator setup, which allows to scan the detector vessel with a 511 keV γ -ray beam. The following chapter discusses the working principle of the collimator setup and a Geant4 Monte Carlo simulation of the detector response.

4.1 The collimator working principle

A 4.5 cm \times 10 cm \times 10 cm lead block, with a hole with diameter 5.0 mm, collimates the γ -ray beam (Figure 28(a)). The ^{22}Na source with an activity of 370 kBq is placed between the collimator and the NaI crystal. An 8 cm \times 8 cm \times 4.5 cm lead block with hole of the diameter 2.54 cm keeps the source in position and shields the detector from escaping γ -rays. The source is at 10 cm distance from the outer vessel, taking into account a small gap between the collimator and the outer vessel. At a distance of 10 cm from the outer vessel, the γ -ray beam has a FWHM of 1.1 cm when it enters the TPC (see Chapter 5.2). Due to the high activity of the ^{22}Na source, pile up of events can occur inside the XAMS TPC and the NaI crystal. To provide shielding from redundant events inside the TPC, the lead collimator is placed next to the outer vessel. To avoid pile up in the NaI crystal, it is at a distance of 10 cm from the source. The setup is placed on a mounting plate with adjustable height to scan the XAMS TPC with the γ -ray beam at different heights.

The radioactive source that emits the γ -rays is ^{22}Na , with a half-lifetime of $t_{1/2} = 2.6\text{ y}$. In 9.64 % of the cases it decays via electron capture, and in 90.3 % of the cases, it decays through β^+ decay:



into the excited $^{22}\text{Ne}^*$ and a neutrino by emitting a positron. The $^{22}\text{Ne}^*$ relaxes into the

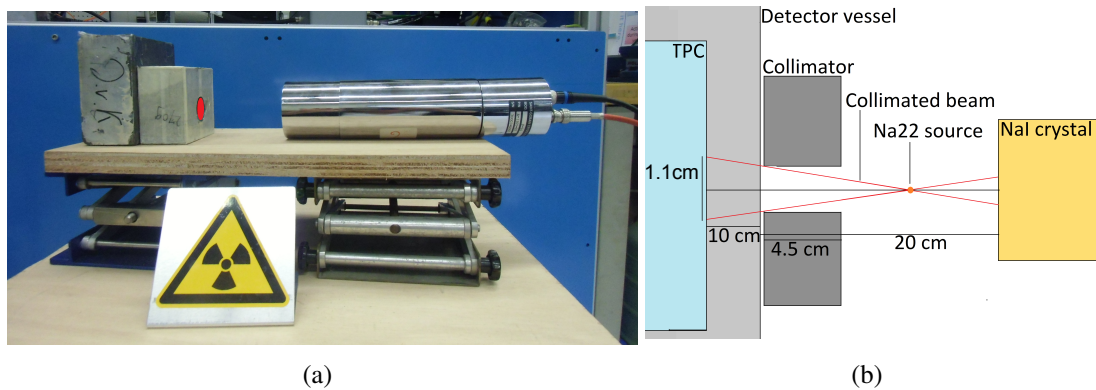


Figure 28: (a) The XAMS collimator setup: The lead collimator is on the left, in the center is the ^{22}Na source (red) in the source holder and on the right is the NaI crystal for external γ -ray trigger. (b) Schematic of the collimator setup. The ^{22}Na is at 10 cm, the NaI crystal at 20 cm from the outer vessel. The FWHM of the beam when it enters the TPC is 1.1 cm. The source holder is not depicted in this scheme.

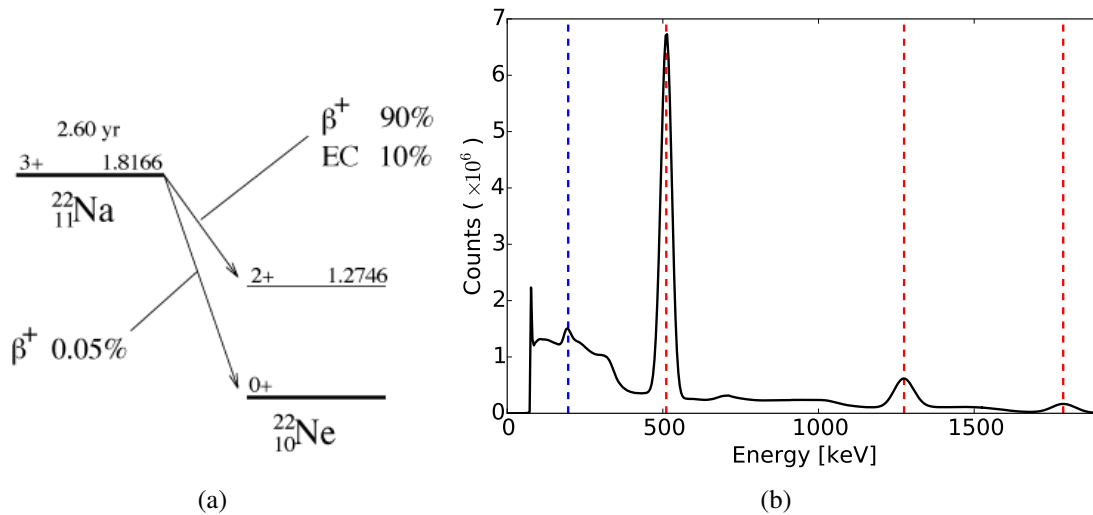
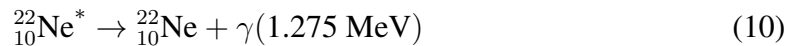


Figure 29: (a) ^{22}Na decay scheme, showing the β^+ decay that occurs with a probability of 90.3 % [45]. (b) ^{22}Na spectrum taken with a NaI crystal. The red dashed lines indicate the γ -ray peaks from the 511 keV and 1275 keV γ -rays as well as their sum peak at 1786 keV. The 511 keV peak shows a clear Compton edge and backscatter peak. The backscatter peak is indicated with the dashed blue line.

stable ^{22}Ne isotope by emitting a 1.275 MeV γ -ray (Figure 29(a)) [45]:



The positron annihilates with an electron of the plastic disc containing the source to two 511 keV γ -rays. Due to the conservation of momentum, the γ -rays are emitted back-to-back. The annihilation is assumed to originate from electrons and positrons at rest, therefore the resulting energy of the gamma rays equals the rest mass of the positron and electron of 511 keV. Figure 29(b) shows the spectrum of ^{22}Na , taken with a NaI crystal. It consists of the 511 keV, the 1275 keV, and the sum peak of both γ -rays at 1768 keV. The 511 keV peak has a clear Compton edge and a backscatter peak. The Compton edge originates from γ -rays, which scatter off electrons and leave the detector, before depositing their total energy. The backscatter peak arises when γ -rays first strike the shielding and then Compton scatter back into the detector.

The XAMS TPC is calibrated with the back-to-back emitted 511 keV γ -rays from the ^{22}Na . Data acquisition is only triggered when one 511 keV γ -ray deposits energy in the NaI crystal and the other one in the TPC. This tight selection of energy depositions of 511 keV in the XAMS detector volume allows an energy recoil calibration of XAMS. The external trigger on the 511 keV γ -rays is performed with a Saint-Gobain 2M2/2 NaI scintillation crystal, several properties are listed in Table 3. A scintillation detector consists of a scintillating material, which generates UV photons in response to incident radiation and a photomultiplier tube which converts the photons into a measurable signal (Figure 30). NaI has a high light yield of 38 000 photons/MeV and a short rise time of 0.5 μs , which make it an efficient detector for γ -radiation. Therefore, the NaI scintillation detector is a suitable crystal to trigger on 511 keV γ -rays in the collimator setup. An event is stored, if a coincident signal between the NaI crystal and the two PMTs inside the TPC occurs.

Property	Value
Crystal diameter	5.08 cm
Operation high voltage	1160 V
Energy resolution	5.1 %
Light yield	38 000 $\frac{\text{photons}}{\text{MeV}}$
Pulse rise time	0.5 μs
Maximum emission	415 nm

Table 3: Properties of the Saint-Gobain 2M2/2 NaI scintillation crystal used for the XAMS collimator setup.

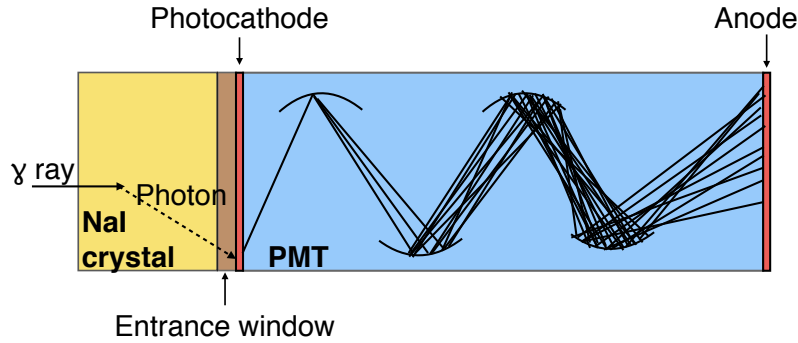


Figure 30: Scheme of a NaI scintillation counter. An incoming γ -ray is converted to a measurable photon in the NaI crystal. In the PMT the photon liberates a photoelectron that is measured as an output voltage.

This occurs, when one back-to-back emitted 511 keV γ -ray deposits energy in the NaI crystal and the other one passes the collimator and deposits energy in the XAMS TPC.

4.2 Attenuation of γ -rays in the XAMS detector material

The event rate of a triple coincidence between the NaI crystal and the two PMTs in the XAMS TPC depends on the opening angle of the collimated beam and the attenuation of the γ -rays in the XAMS detector material. For the source at 10 cm distance from the outer vessel, the collimator reduces the event rate to 0.016 % of the activity of the source. Three effects are involved in the attenuation of the γ -rays in the matter: the photoelectric effect, Compton scattering and pair production. With the photoelectric effect the γ -ray loses all of its energy in one interaction. The probability for this process to happen depends strongly on the energy of the γ -ray and is most effective in material with high atomic number Z . The photo electric effect is relevant for γ -rays in the energy range below 1 MeV. With Compton scattering, the γ -ray loses only part of its energy in one interaction. The energy is lost when the γ -ray scatters off an electron of the material it passes and is relevant for γ -rays in the range between 100 keV and 10 MeV. High energy gamma rays can also lose energy via pair production. Pair production is the effect when a photon creates an electron-positron pair near a nucleus. Which type of interaction dominates depends of the energy of the γ -ray and the material it traverses. Before the γ -rays enter the XAMS TPC, they have to pass 0.6 cm of stainless steel from the inner and outer

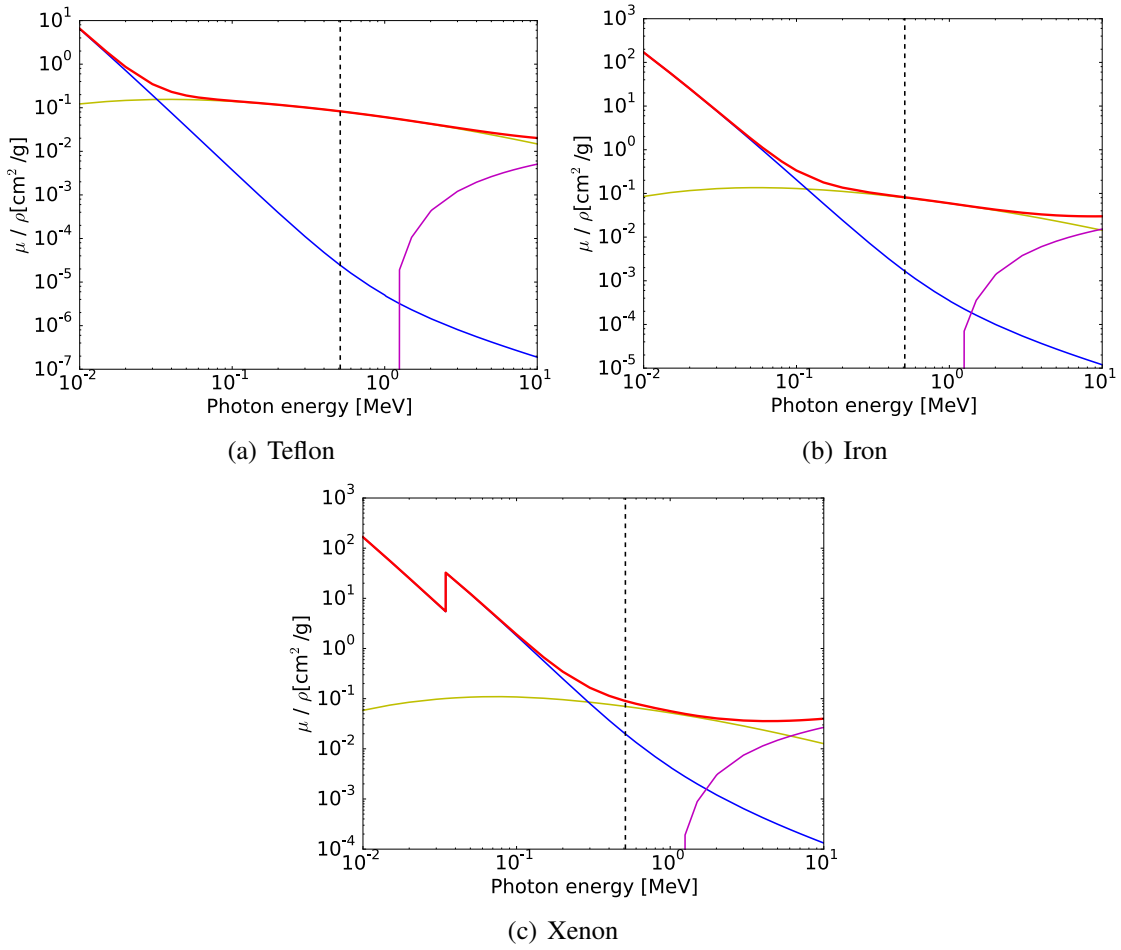


Figure 31: Mass attenuation coefficient of (a) Teflon, (b) iron and (c) xenon for the photoelectric effect (blue), Compton scattering (yellow), pair production (magenta) and the total attenuation from all contributions (red) [46], the dashed black line indicates 511 keV. The most dominant effect for the absorption of 511 keV γ -rays in stainless steel, xenon and Teflon is Compton scattering.

vessel walls, a 0.2 cm thin layer of liquid xenon and 4.6 cm of Teflon. Figure 31 shows the mass attenuation coefficient $\frac{\mu}{\rho}$ of Teflon, xenon and iron (stainless steel consists of more than 80 % of iron), depending on the energy of the incoming γ -ray. The mass attenuation coefficient is a quantity that characterises how easily a material can be penetrated by a γ -ray:

$$I(x) = I_0 e^{(-\frac{\mu}{\rho} \rho x)}, \quad (11)$$

where I_0 is the incoming and $I(x)$ the outgoing intensity of a γ -ray that traverses a material with length x and density ρ . In Teflon and iron, the probability for 511 keV γ -rays to interact via Compton scattering dominates, in xenon Compton scattering and photoelectric absorption are equally relevant. Pair production does not occur at this low energy. With Equation 11 the γ -ray event rate of the 370 kBq ^{22}Na source with the collimator setup is estimated to be 15.6 Hz. This deviates from the measured event of 23 Hz rate by 32 %. For a more accurate calculation of the expected event rate in the XAMS TPC after the attenuation of the γ -rays is simulated in Geant4.

4.3 Geant4 Monte Carlo simulation of the collimator setup

Geant4 is a toolkit developed by CERN to simulate the passage of particles through matter by using Monte Carlo methods [47]. In the Geant4 framework, the XAMS detector and the collimator geometry are modelled in a simplified version of the actual detector setup. The goal of the simulation is to determine how strong the γ -rays from a ^{22}Na source are attenuated in the detector material and what the expected detector response is, given a coincidence trigger between the NaI crystal and the XAMS PMTs. For this purpose, the detector geometry of XAMS is simplified to the liquid xenon TPC, surrounded by the Teflon holding structure, that is placed inside the inner and outer stainless steel vessel. Between the Teflon structure and the inner vessel there is a thin layer of liquid xenon and between the inner and outer vessel there is vacuum (Figure 32). These are the main parts of XAMS that have to be taken into account for the attenuation of the γ -rays. The collimator setup consists of the collimator next to the outer vessel, taking into account a small gap between the outer vessel and collimator, the NaI crystal at a distance of 10 cm from the outer vessel and the ^{22}Na source inside the lead source holder between the collimator and the NaI crystal. The sensitive detector elements of the simulation are the liquid xenon inside the Teflon structure and the NaI crystal. Each generated ^{22}Na particle decays into a β^+ particle, one 1.275 MeV γ -ray and one neutrino, taking into account a branching ratio of 90 %. The β^+ annihilates with an electron in the plastic of the source disk to two

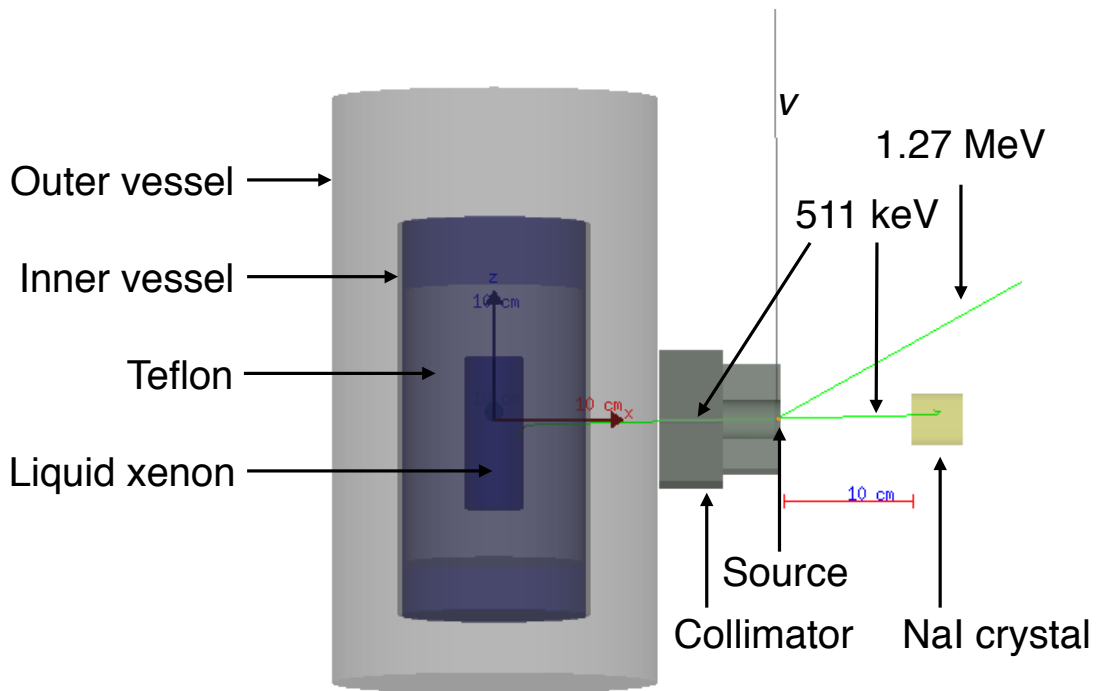


Figure 32: On the left: Detector geometry of XAMS with the outer and inner vessel, a xenon layer, the Teflon structure and the sensitive liquid xenon (from outside to inside). On the right: Collimator setup with collimator, source holder, source and NaI crystal (yellow) (from left to right). The displayed event is a ^{22}Na event, γ -rays are displayed in green, the neutrino in grey. One 511 keV γ -ray enters the TPC, the other one is absorbed by the NaI crystal and the 1275 keV γ -ray does not interact with any detector material.

back-to-back emitted 511 keV γ -rays (Figure 32).

Two physics models are implemented in the simulation: the hadronic physics model *G4QGSP_BERT* and the low energy electromagnetic physics model *emlivermore*. The Geant4 physics builder *G4RadioactiveDecayPhysics* simulates the radioactive decay of the ^{22}Na . The hadronic model manages elastic and inelastic hadron and ion interactions with atomic nuclei for high energy physics applications and is of minor relevance for the comparable low energies of the ^{22}Na decay products. The interaction of the low energy γ -rays at XAMS are modelled with the *emlivermore* physics list, which is designed for applications that require a high accuracy of electron and photon interactions with matter in an energy range between 250 eV and 1 GeV [48]. Among others it covers the simulation of interactions through the photo-electric effect and Compton scattering; the interaction channels that are relevant for the absorption of the ^{22}Na decay products.

For the Monte Carlo data set, 196×10^6 ^{22}Na decays are generated. With a 370 kBq strong source this corresponds to a measurement period of 8.8 min. Only those events, that give an energy deposit over a energy threshold from a comparable measurement in the NaI crystal and in the liquid xenon are kept in the Monte Carlo data set. The total resulting simulated event rate of coinciding energy depositions in the NaI crystal and the XAMS TPC is 22.8 Hz, which only deviates by 0.9 % from the measured event rate of 23.0 Hz.

5 Detector characterisation

The two signals measured with the XAMS dual-phase xenon time projection chamber are the prompt scintillation light S1 and the proportional S2 signal. The efficiency with which these signals are detected, determines the quality of the performance of the detector. For the calibration, two radioactive sources are used: a 191.2 kBq ^{137}Cs and a collimated, 370 kBq ^{22}Na source. Data acquisition with the ^{137}Cs source is triggered with a coincidence in the bottom and top PMT, the acquisition with the ^{22}Na source is triggered with a coincidence between the top PMT, the bottom PMT and an external NaI crystal.

5.1 Event selection for data analysis

Each data set underlies at least two posteriori cuts: First, only events with at least one S1 and one S2 peak are considered in the analysis. Second, only events with a drift time between 0 and 60 μs are accepted in the analysis, since the maximum drift time for electrons at XAMS with a drift field of 0.6 kV cm^{-1} does not exceed 60 μs (Figure 33). The events outside the acceptance region between 0 and 60 μs contain multiple S1 and S2 signals from pile up. For the drift time calculation the maximum S1 and S2 signal of each event are used. For pile up inside the events, these can originate from different interactions, which results in an incorrect drift time. These events are excluded from the analysis in each data set.

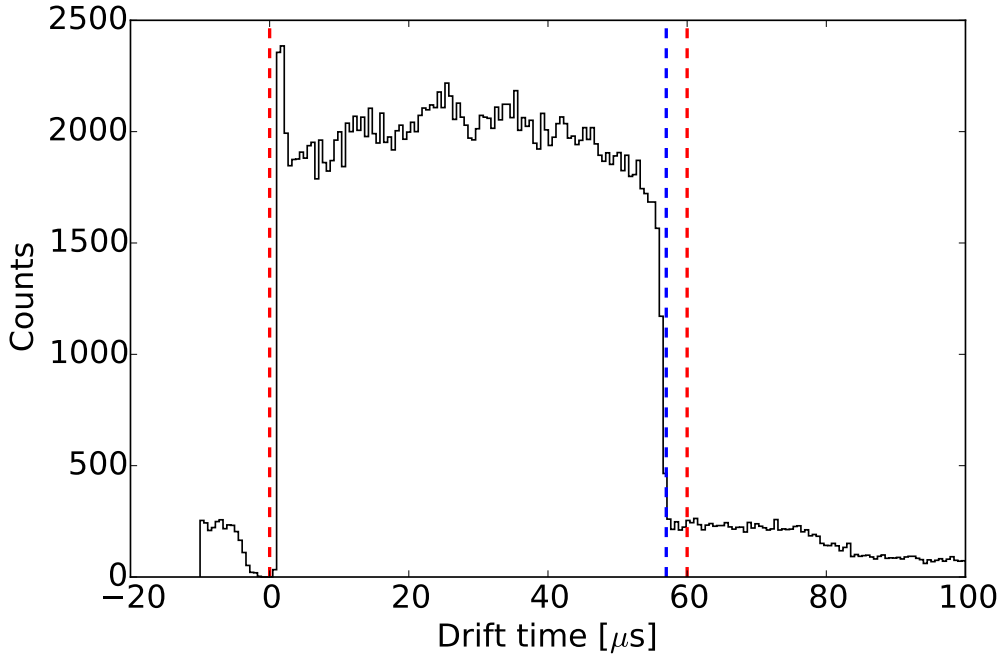


Figure 33: Electron drift time at XAMS measured with a ^{137}Cs source at a drift field of 0.6 kV cm^{-1} and a height of the liquid level above the gate mesh of 2 mm. The events outside the acceptance region between 0 and 60 μs (red, dashed line) contain multiple S1 and S2 signals from pile up. These events are excluded from the analysis. The maximum drift time of $57 \pm 1\ \mu\text{s}$ is indicated with the dashed blue line.

Furthermore, there are two optional cuts applied, depending on the data set. The first optional cut removes events with a double scatter peak in the S2 signal. This occurs, when the incoming γ -ray from the radioactive source scatters in the liquid xenon and deposits energy at more than one point in the TPC. If the scatter points are sufficiently separated in the z -coordinate, two S2 peaks are observed. Since for the analysis, only the main S1 and the main S2 are taken into account, double scatter occurrences in the S2 signal falsify the analysis. The corresponding S1 signals are observed simultaneously, due to their transmission with the speed of light and the finite energy resolution of the digitizer. Finally an optional cut that is based on asymmetry studies can be deployed, it is explained in detail in Chapter 5.3. It removes misstaged and not fully recorded events due to PMT saturation from the analysis. A summary over the acceptance of the different cuts is displayed in Table 4.

Cut type	Events ^{137}Cs measurement	Events ^{22}Na measurement
None	281 093 (100 %)	136 189 (100 %)
At least one S1 and one S2	250 856 (89 %)	129 203 (95 %)
Drift time between 0 and 60 μs	201 329 (72 %)	121 168 (89 %)
Compton Scatter	148 892 (53 %)	97 492 (72 %)
Asymmetry	131 794 (47 %)	91 706 (67 %)

Table 4: Subsequently applied cuts to the data set for the ^{137}Cs and the collimated ^{22}Na measurement at XAMS and the corresponding acceptance with respect to the total number of events.

5.2 Interaction depth and collimator beam width

The interaction depth is the z position at which the incoming γ -ray interacts with the liquid xenon. It is calculated from the drift time by taking the time difference between the S1 peak maximum and the beginning of the S2 peak. It depends on the strength of the drift field and the depth of the interaction below the liquid-to-gas interface. The deeper down in the TPC the interaction occurs, the longer is the drift time. The minimum measured drift time depends on the threshold for the minimum gap size set in the pax clustering algorithm and is set to 1.0 μs , the maximum drift time depends on the length of the TPC and the strength of the drift field. In XAMS, the standard drift field during operation with liquid xenon is 0.6 kV cm^{-1} , with a maximum drift time of 57.0 μs at a height of the liquid level 2.0 cm above the gate mesh. Assuming that the electrons from the ionisation interaction are accelerated in an negligible amount of time, the interaction depth $D(t_d)$ depending on the drift time t_d and the drift velocity v_d is calculated with

$$\begin{aligned} D(t_d) &= t_d v_d \\ &= t_d \frac{l_{TPC}}{t_{d,max}}, \end{aligned} \quad (12)$$

where l_{TPC} is the full length of the TPC and $t_{d,max}$ is the maximum drift time at a certain drift field.

Figure 34 shows the interaction depth of a collimated 511 keV γ -ray beam from the ^{22}Na source, that is aimed at the center of the TPC. In order to be comparable to the

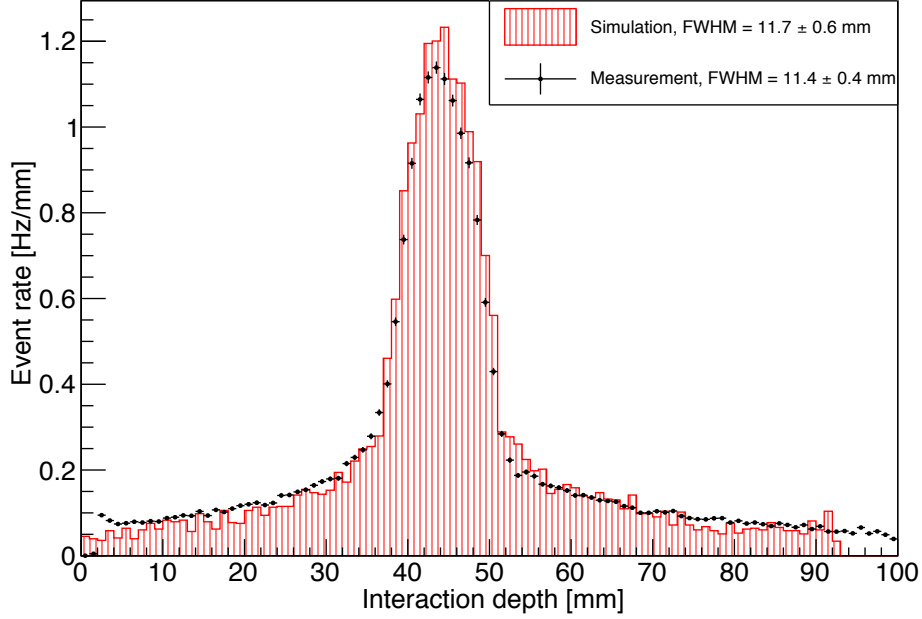


Figure 34: Comparison of the simulated interaction depth (red) with the interaction depth of a collimated 511 keV γ -ray from a ^{22}Na source (black). The measured γ -ray beam has a full width of half maximum (FWHM) of 11.4 ± 0.4 mm, which only deviates from the FWHM of the Monte Carlo generated γ -ray beam of 11.7 ± 0.6 mm by 2.6 %.

simulated data, only events with at least one S1 and S2 and a drift time between 0 and $60 \mu\text{s}$ are considered in the analysis. The unscaled Monte Carlo simulation is displayed in red. The simulation has been aligned with the mean value of the measured peak. The simulated and the measured beam width are in very good agreement.

5.3 Top-bottom asymmetry

The top-bottom asymmetry A_{tb} is a measure for the relative light collection per PMT and it is defined as:

$$A_{tb} = \frac{n_t - n_b}{n_t + n_b}, \quad (13)$$

where n_t is the number of photoelectrons detected by the top PMT, and n_b the number of photoelectrons detected by the bottom PMT. The top-bottom asymmetry ranges from -1 to 1 , where a negative value indicates that most of the light is collected by the bottom PMT and a positive value indicates that more light is collected by the top PMT.

Figure 35 shows the S1 asymmetry versus the S2 asymmetry of the ^{137}Cs source. Events in the main band are inside the red rectangle, where the S2 asymmetry is constant at 0.04 and the S1 asymmetry ranges from -0.9 to -0.45 . Events in the dashed green rectangle fall below the main band due to saturation effects in the top PMT [38]. The events in this population have S2 events which are bigger than the saturation threshold of the top PMT of about 8000 photoelectrons. Therefore, the amount of photoelectrons detected by the bottom PMT seems to be larger than the amount of photoelectrons detected by the top PMT. As a result, the S2 asymmetry drops towards the bottom PMT. The events in the

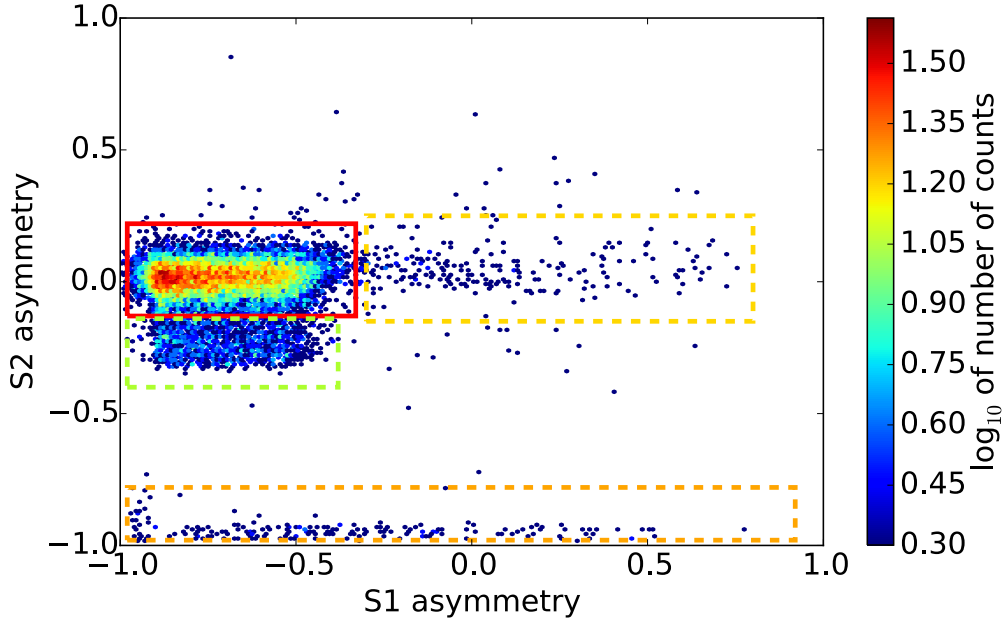


Figure 35: Density plot of the S1 and S2 asymmetry from the ^{137}Cs source. The main band (red rectangle) is at a constant S2 asymmetry of 0.04 and the S1 asymmetry ranges from -0.9 to -0.45 . The events in the dashed green box fall outside the main band due to saturation effects in the top PMT. The events in the dashed yellow box are events where a small S2 peak is mistagged as S1 peak, while the events in the dashed orange box are wide noise occurrences in the bottom PMT which are mistagged as S2 peaks. All events except those in the main band are excluded from the following analysis.

dashed, yellow rectangle contain very wide S1 peaks. These S1 peaks are actually small S2 peaks, that are mistagged by the classification algorithm. The events contained in the dashed, orange rectangle stand out because they seem to have S2 signals close to the bottom PMT. Nevertheless, it was found that the bottom PMT is noisy. The peaks originating from electrical noise are mistagged as S2 peaks, and are therefore contributing to the plot. For the cut based on the asymmetry, all events inside the dashed rectangles are excluded from the analysis.

Figure 36 shows the top-bottom asymmetry of the S1 (grey rectangle) and the S2 signal (black rectangle) of the ^{137}Cs source, depending on the drift time. The full set of cuts has been applied to this data set. The S2 signal is produced when electrons from the interaction emit photons in the amplification area above the liquid-to-gas interface, independent of the interaction depth in the TPC. Thus, the top PMT always detects more photons from the S2 signal. The lower, decreasing band is from the S1 signal. In general, the S1 scintillation light is more detected by the bottom PMT. This is because liquid xenon has a higher refraction index than gaseous xenon. Thus, the probability of the scintillation light to be reflected at the liquid-to-gas interface and then detected by the bottom PMT is high. The amount of light that is detected by the bottom PMT depends on the position of the interaction. The deeper down in the TPC the scintillation light is emitted, the closer the interaction point is to the bottom PMT and therefore the bigger the solid angle is to the bottom PMT. Therefore, less light is absorbed by scattering effects at the Teflon walls.

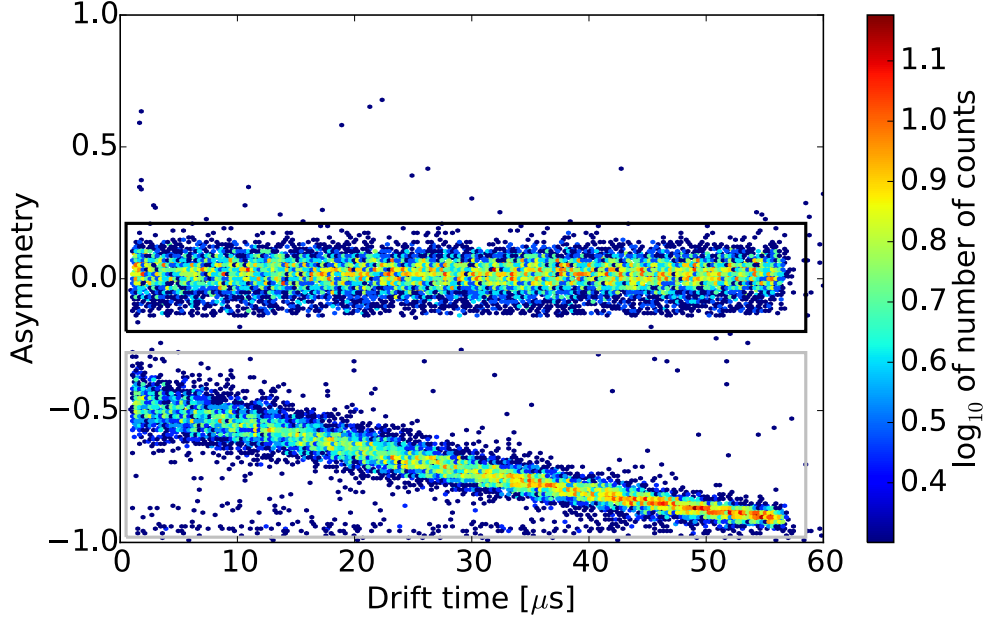


Figure 36: S1 (grey rectangle) and S2 asymmetry (black rectangle) from a ^{137}Cs source depending on the drift time. The S2 events are more detected by the top PMT, since the proportional signal is emitted in the amplification area. The S1 events are more detected by the bottom PMT as the interaction position in the TPC decreases, since photon loss due to reflections at the teflon walls get less and the solid angle to the bottom PMT increases.

The fraction of the collected light to the amount of emitted photons is called the light collection efficiency (see Chapter 5.6).

5.4 S2 broadening

The influence of the interaction depth on the S2 signal is reflected in the S2 broadening. The S2 broadening is the increase of the width of the S2 signal with increasing drift time. It is caused by longitudinal diffusion of the electrons during their drift in the TPC and the average proportional scintillation distribution from the single electrons in the amplification area. For events with a drift time $t_d > 30 \mu\text{s}$, the measured S2 width σ_e can be expressed in the following way:

$$\sigma_e = \sqrt{\frac{2D_L t_d}{v_d^2} + \sigma_0^2}, \quad (14)$$

where D_L is the longitudinal diffusion coefficient, t_d the drift time and σ_0 a free parameter [49].

Figure 37 shows the distribution of increasing S2 width measured from a ^{137}Cs source depending on the drift time. All cuts were deployed in this data set, which leaves 47 % of the events in the analysis. At a drift field of 0.6 keV and a drift velocity of $1.789 \text{ mm } \mu\text{s}^{-1}$, a longitudinal diffusion coefficient of $D_L = (6.9 \pm 0.1) \times 10^{-4} \frac{\text{mm}^2}{\mu\text{s}}$ is obtained from a fit of Equation 14 to points with $t_d > 30 \mu\text{s}$. The longitudinal diffusion coefficient

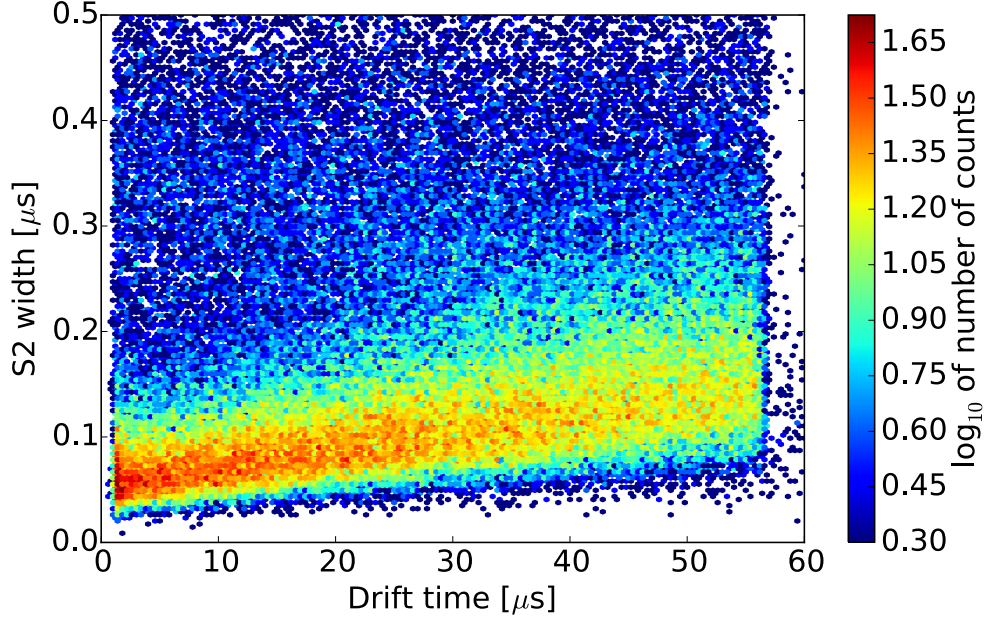


Figure 37: Broadening of the S2 signal from a ^{137}Cs source with increasing drift time. The fit of Equation 14 to the data points with $t_d > 30 \mu\text{s}$ gives a longitudinal diffusion coefficient of $D_L = (6.9 \pm 0.1) \times 10^{-4} \frac{\text{mm}^2}{\mu\text{s}}$, with an applied drift field of 0.6 keV and a drift velocity of $1.789 \text{ mm } \mu\text{s}^{-1}$.

from the XENON100 experiment is $D_L = (10.74 \pm 0.15) \times 10^{-4} \frac{\text{mm}^2}{\mu\text{s}}$ at a drift field of $E_d = 0.53 \frac{\text{kV}}{\text{cm}}$ [50]. D_L depends on the applied drift fields, it decreases in value for higher drift fields [49]. In this context the longitudinal diffusion coefficient of XAMS agrees with the diffusion coefficient obtained at XENON100, as the drift field applied at XAMS is 13 % higher than the field applied at XENON100.

5.5 Electron lifetime

For the S2 signal, the electrons from the ionisation interactions are drifted towards the gate mesh in the TPC. During the duration of the drift, the electrons can attach to impurities in the liquid xenon. Assuming a uniform distribution of impurities, the number of electrons surviving after drifting for a certain time t_d , $S2(t_d, E)$, from an initial number of electrons $S2(0, E)$, is given by

$$S2(t_d, E) = S2(0, E)e^{-\frac{t_d}{\tau_e}}, \quad (15)$$

where τ_e is the electron lifetime. The electron lifetime is therefore the mean time an electron drifts freely through the TPC before it is absorbed. The higher the lifetime, the less impurities are in the liquid xenon.

From Equation 15, a correction for the S2 area can be obtained. Therefore, the TPC is scanned with the collimated 511 keV γ -ray beam from the ^{22}Na source at five equidistant positions below the gate mesh (Figure 38). Each position corresponds to a separate measurement and to each resulting data set the all cuts are applied. At each collimator position the drift time and the S2 area are calculated. The 511 keV photopeak is visible at

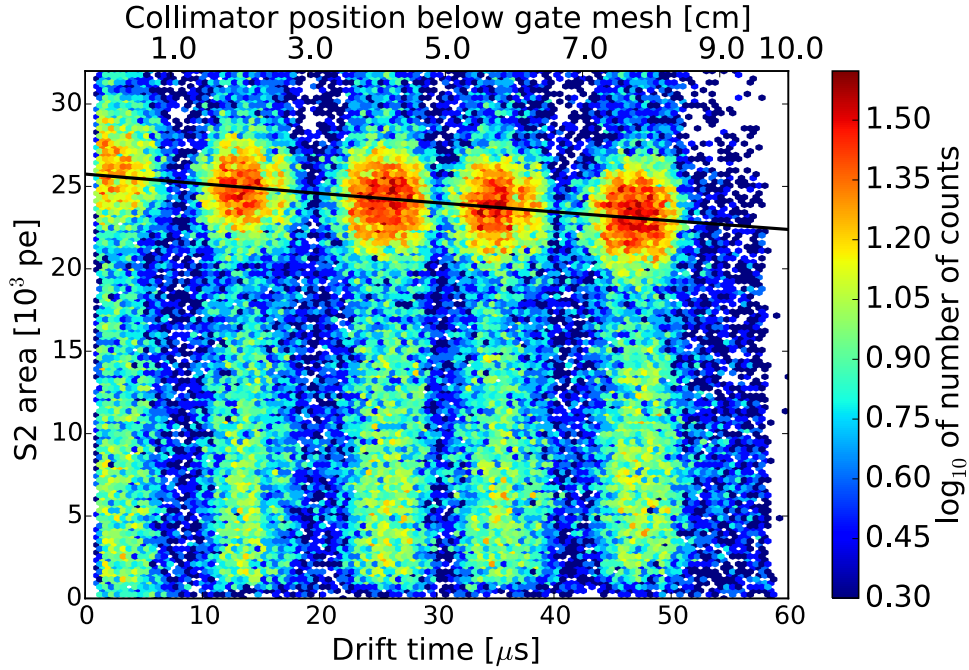


Figure 38: S2 area depending on the drift time for a collimated 511 keV γ -ray beam aimed at five different positions in the TPC after purifying 7.3 kg of xenon for 7 days during run 7. The black curve shows the fit of Equation 15 to the data points ($\frac{\chi^2}{NDF} = \frac{24}{9}$), resulting in a electron lifetime of $429 \pm 26 \mu\text{s}$ and a correction factor for the S2 signal of $S2(0, E) = 25747 \pm 100 \text{ pe}$.

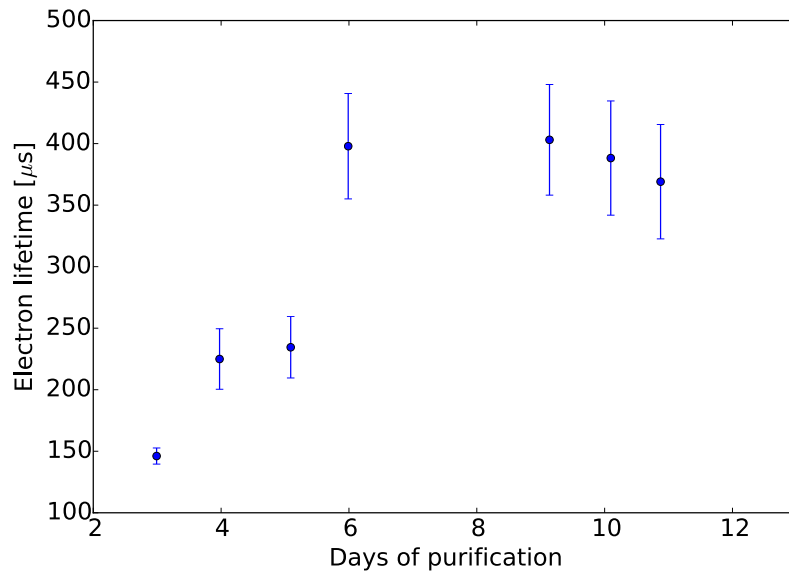


Figure 39: Increasing trend of the electron lifetime during constant purification of the xenon during run 6, measured with a ^{137}Cs source over several days. After purifying the xenon for three days already less than 32 % of the electrons from events occurring at the bottom of the TPC are absorbed by impurities.

large S2 areas together with a Compton edge at small S2 areas. The measured photopeak position in the TPC deviates up to 1 cm in the most extreme case from the height of the γ -ray beam. This is because the externally measured collimator position with respect to the gate mesh underlies systematic uncertainties like the determination of the gate mesh position at cryogenic temperatures from the outside of the detector and the possibility that the γ -ray beam underlies a tilt due to misalignments in the collimator setup.

Furthermore, the electron lifetime is a measure for the purity of the xenon. Figure 39 shows the increasing trend of the electron lifetime while purifying during run 6. The electron lifetime is measured with a ^{137}Cs source. With Equation 15 it can be calculated, that after purifying the xenon for three days, less than 32 % of the electrons from interactions occurring at the bottom of the TPC get absorbed by impurities.

5.6 Light collection efficiency

The amount of light from the S1 scintillation signal of a certain energy deposition, that is detected at the PMTs, depends on the *light collection efficiency* (LCE). The light collection efficiency in turn depends on the position of the interaction in the active region, reflectivity of the TPC walls, light reflections at the liquid-to-gas interface, solid angle effects, transmission of the field meshes and the Rayleigh scattering length. The closer the interaction occurs to the PMTs, the more light is collected by them. This effect is shown in Figure 40, where the S1 area is shown as a function of drift time. All cuts are applied to the data set. The five peaks at different drift time positions are obtained from the collimated 511 keV γ -rays from the ^{22}Na source at five equidistant positions below the

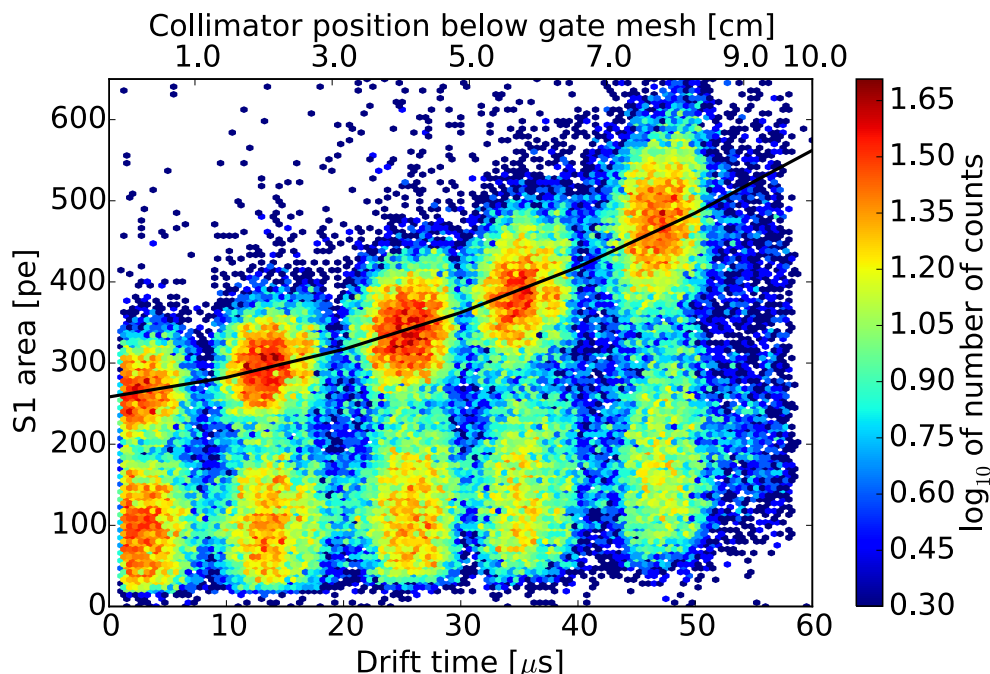


Figure 40: S1 area depending on the drift time from a scan of the XAMS TPC with the collimated 511 keV γ -ray beam. The black curve is the quadratic fit to the photopeak, giving the correction function for the light collection efficiency. The fit values are displayed in Table 5.

gate mesh. The 511 keV photopeak is visible at large S1 areas, whereas the peak at low S1 area corresponds to the Compton scatter peak of the 511 keV γ -rays. For an increasing drift time, that is an increasing distance of the collimator to the gate mesh, the S1 area of the photopeak increases significantly. Therefore, a position dependent correction of the S1 area has to be applied when measurements from different positions within the TPC are compared with each other. For XAMS a correction function for the light collection efficiency can be calculated, depending only on the depth of the interaction in the TPC. The correction function is obtained by fitting the S1 area of several 1 μ s wide drift time slices of each photopeak to a quadratic polynomial, depending on the drift time t_d . The resulting fit is depicted as the black curve in Figure 40, the fit values are displayed in Table 5. With this correction function, the light collection efficiency increases by a factor 2.1 across the TPC, with the largest value for interactions at the bottom PMT and the minimum value for interactions at the liquid-to-gas interface. In the following analysis the S1 area is corrected with the obtained correction map.

Variable	Value	Error
a_0	2.58×10^2	2.00
a_1	1.87	2.08×10^{-1}
a_2	5.34×10^{-2}	4.60×10^{-3}

Table 5: Values obtained from the fit of the quadratic equation $f(x) = a_0 + a_1x + a_2x^2$ to the data points. The fit returns $\frac{\chi^2}{NDF} = \frac{46}{35}$.

5.7 S1 light yield

Knowing the correction function for the light collection efficiency, a volume averaged light yield for XAMS can be calculated. The light yield is a property of scintillation counters, and describes how many photo electrons are detected per deposited unit energy. In XENON100, the volume average light yield is the reference value for the relative light yield [27]. At a drift field of 0.6 kV cm^{-1} the volume averaged light yield of XAMS with an energy of 511 keV from the ^{22}Na source of the incident γ -ray is $L_y = 0.73 \pm 0.03 \text{ pe/keV}$. The light yield depends on several different factors, like the light collection efficiency, the fraction of light detected by the PMTs (LCE), the quantum efficiency of the deployed PMTs (QE), the applied electric field and the energy of the incoming γ -ray, and can be approximated with:

$$L_y = n_{\text{photons}}(\text{Energy, El. field}) \cdot \text{LCE} \cdot \text{QE}. \quad (16)$$

The number of photons produced per interacting unit energy can be calculated with NEST, a simulation tool for the simulation of scintillation and electroluminescence processes in liquid noble elements [51]. For an incoming γ -ray of 511 keV at an electric field of 0.6 kV cm^{-1} the number of produced photons is 28.4 photons/keV and for an incoming γ -ray of 122 keV at zero electric field it is 63 photons/keV. With this the XAMS light yield at zero electric field with an γ -ray energy of 122 keV can be calculated to be $1.64 \pm 0.09 \text{ pe/keV}$. The light yield at XENON100 under the same conditions is 4.3 pe/keV [52]. The main reason for the difference of the light yields of the two experiments by a factor 2.7 is the different geometry. While XENON100 has a diameter to width

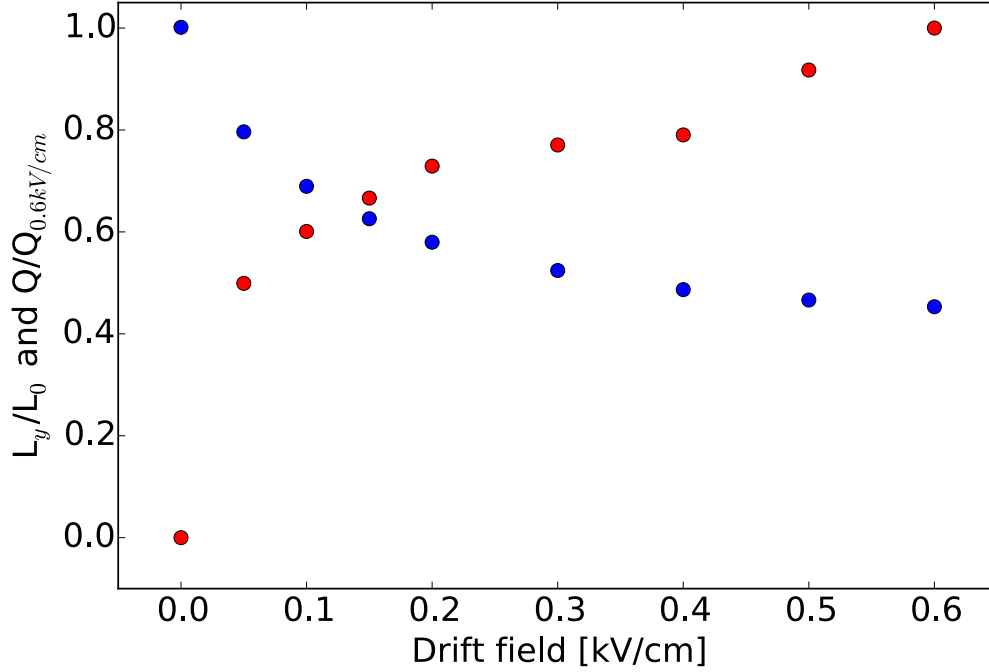


Figure 41: Light yield L_y with respect to the light yield at zero drift field L_0 (blue) and corresponding S2 area scaled with the S2 area at the maximum drift field of the collimated ^{22}Na source. The error bars are a fraction of the marker size. With increasing drift field, the light yield decreases, while the S2 area increases. This is because less electrons recombine with the xenon ions, which results in a smaller S1 area but a bigger S2 area.

ratio of 1, XAMS has a diameter to width ratio of 0.4. The light in the much narrower and longer XAMS TPC undergoes much more reflections than light in XENON100, before it is detected by the PMTs. The smaller light collection efficiency at XAMS thus results in a smaller light yield.

Furthermore, the light yield depends on the strength of the applied drift field, since recombining electrons contribute to the scintillation light. Figure 41 shows the ratio of L_y with respect to the scintillation yield L_0 (blue) at zero field and the S2 area at different fields scaled with the S2 area at the maximum drift field of 0.6 kV cm^{-1} as functions of the drift field. As the drift field increases, the number of recombining electrons decreases. As a result the number of photons that contribute to the S1 signal decreases while the number of electrons contributing to the S2 signal increases. The plateau in the S2 area at 0.2 kV cm^{-1} and 0.3 kV cm^{-1} is an artefact of the normalisation with $Q_{0.6 \text{ kV/cm}}$. The measurement at 0.6 kV cm^{-1} was found to have a lower liquid level than the other measurements. A lower liquid level means a bigger amplification area for the S2 signal, which results in a higher S2 area. The S2 area for 0.6 kV cm^{-1} is therefore bigger than it would have been with the same height of the liquid level as the other measurements. Nevertheless, the cathode scan shows the increasing S2 area and decreasing S1 area with changing drift field. The effect that the S1 area is anti-correlated with the S2 area is used to obtain the combined energy scale of the detector.

5.8 Combined energy scale

In liquid xenon the S1 and the S2 signal are anti-correlated. The anti-correlation is an artefact of the applied electric field. If no electric field is applied, all electrons recombine and contribute to the scintillation light. The stronger the electric field, the more electrons are drifted away from the interaction point. As a result, the S2 signal gets bigger while the S1 signal gets smaller. To fulfil the energy balance, the two signals are therefore anti-correlated. This anti-correlation effect has to be taken into account when the energy resolution of the detector is determined. The combined energy scale (CES) of the S1 and S2 signal gives an estimator for the best energy resolution of the detector. Figure 42 shows the ^{22}Na calibration data, taken at the center of the TPC, in the S1-S2 parameter space. In order to be comparable to the simulation, only the minimum amount of cuts with events that at least have one S1 and one S2 and a drift time between 0 and $60\mu\text{s}$ are used on the data set. Furthermore, the data set contains the light yield and the electron lifetime corrected S1 and S2 area. The anti-correlation of the S1 and the S2 photopeak is indicated by the ellipse in the upper right corner of the plot, the low energy tail corresponds to Compton scattering and is therefore excluded from the fit. A projection along the anti-correlation ellipse leads to an improved energy resolution. The projection is obtained in the following way: The anti-correlation ellipse from Figure 42 is fit to a bivariate gaussian,

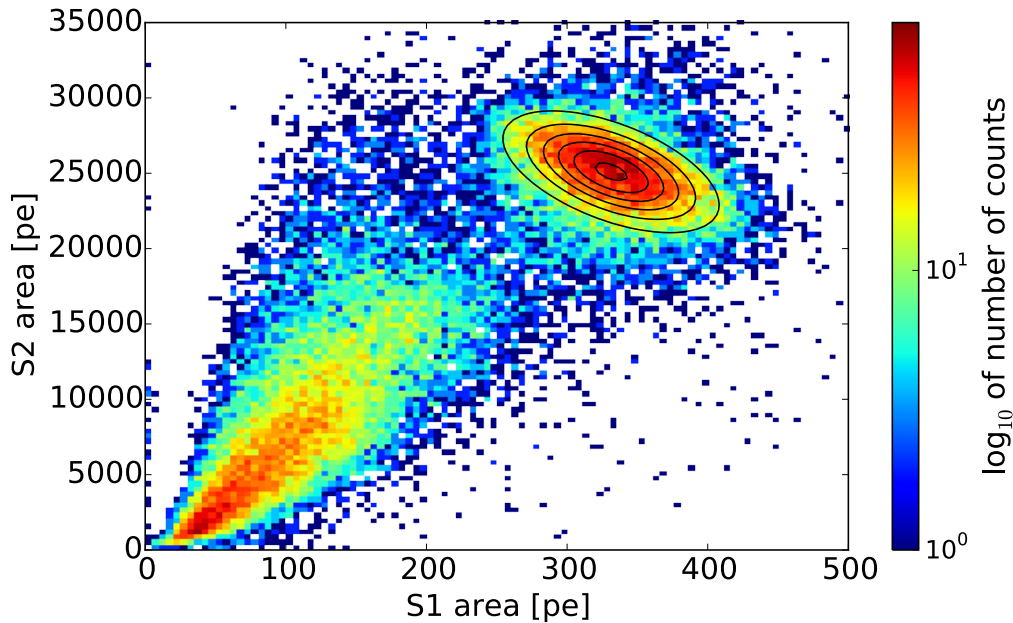


Figure 42: ^{22}Na calibration data in the S1-S2 parameter space. The anti-correlation of the signals is obtained from a fit of a bivariate gaussian to the S1-S2 photo peak (black). A projection along the short axis of the anti-correlation ellipse leads to the best energy resolution of the detector. The events at low energies are the Compton edges of the S1 and the S2 signal.

which takes into account the anti-correlation of the S1 and the S2 area:

$$f_{\mathbf{x}}(x, y) = \frac{1}{\sqrt{(2\pi)^k |\mathbf{E}|}} \exp\left(-\frac{1}{2}(\mathbf{x} - \boldsymbol{\mu})^T \mathbf{E}^{-1}(\mathbf{x} - \boldsymbol{\mu})\right) \quad \text{where} \quad (17)$$

$$\boldsymbol{\mu} = \begin{pmatrix} \mu_x \\ \mu_y \end{pmatrix} \quad \text{and} \quad \mathbf{E} = \begin{pmatrix} \sigma_x^2 & \rho\sigma_x\sigma_y \\ \rho\sigma_x\sigma_y & \sigma_y^2 \end{pmatrix},$$

with the width of the S1 signal σ_x , the width of the S2 signal σ_y , the x and y position of the center of the ellipse μ_x and μ_y and the correlation parameter ρ . From the correlation factor ρ , the rotation angle θ of the ellipse can be calculated by comparing the ellipse equation in the exponent of Equation 17 to the equation of a rotated ellipse. Projecting the anti-correlation ellipse along the short ellipse axis gives the combined energy scale of S1 and S2 signal with the best resolution.

Figure 43(a) shows the combined energy scale of the XAMS TPC. The energy resolution $\frac{\sigma_E}{E}$ at 511 keV of the S1 spectrum is $15.9 \pm 0.3 \%$, of the S2 spectrum $9.9 \pm 0.5 \%$ and for the combined energy scale $6.7 \pm 0.3 \%$. By multiplying the number of produced photons per unit energy from NEST with the light yield from XAMS and assuming a poisson distribution of the emitted photons, an expected resolution of $20.1 \pm 0.4 \%$ is obtained for the S1 signal. The reason for the difference between the measured and the expected resolution lies in the PMT gain that is used in the processing softwar for the calculation of the number of photo electrons for the S1 area. Since the PMTs were calibrated at room temperature, a change in the gain at cryogenic temperatures can not be excluded. Furthermore it was found, that by slightly varying the anti-correlation angle an even better energy resolution of the combined energy scale of $4.9 \pm 0.1 \%$ could be achieved (Figure 44). The resolution obtained with the fit of the bivariate gaussian and the resolution from the

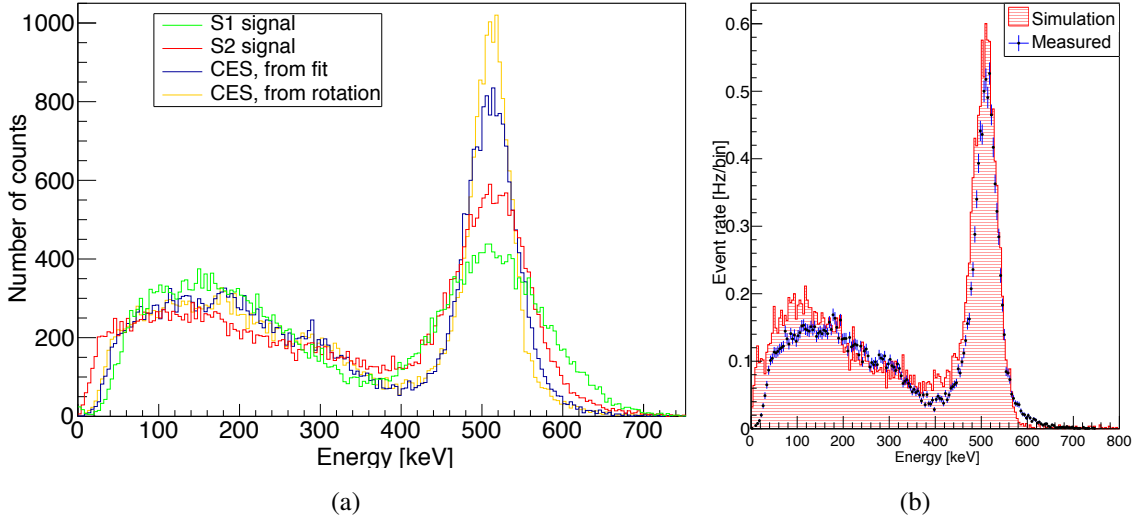


Figure 43: (a) Spectrum of ^{22}Na at 511 keV at four different energy scales: The resolution $\frac{\sigma_E}{E}$ is $15.9 \pm 0.3 \%$ for the S1 spectrum, $9.9 \pm 0.5 \%$ for the S2 spectrum, $6.7 \pm 0.3 \%$ for the combined energy scale (CES) from the fit to the bivariate gaussian and $4.9 \pm 0.1 \%$ for the combined energy scale from variation of the rotation angle. (b) Comparison of the best combined energy spectrum to the Monte Carlo simulation. The simulation and the measurement are in very good agreement.

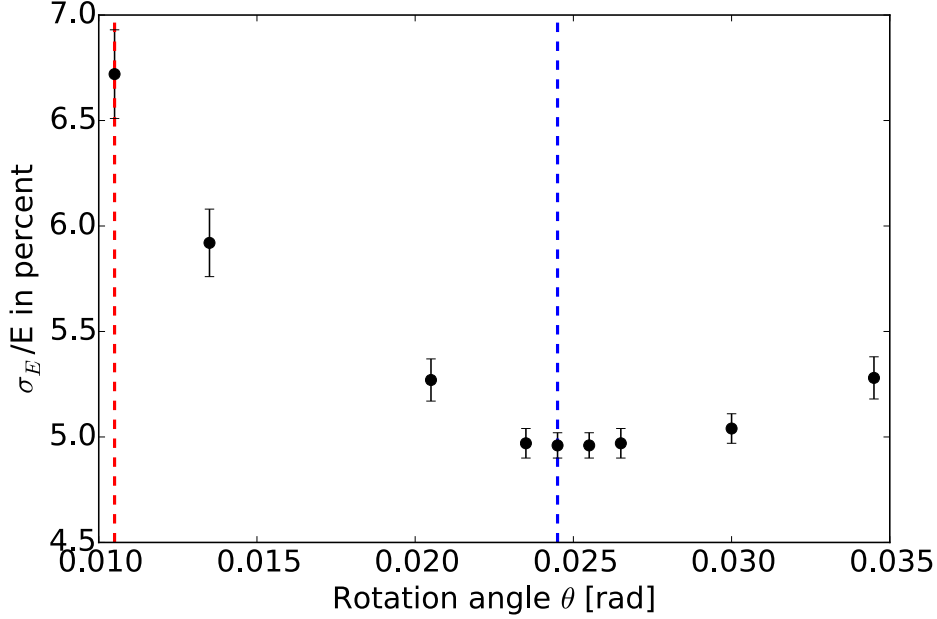


Figure 44: Variation of the rotation angle θ in order to determine the best energy resolution of XAMS. The red dashed line indicates the resolution found through the fit of the bivariate gaussian to the S1 and S2 area, the blue dashed line indicates the rotation angle that gives the best value for the energy resolution of 4.9 ± 0.1 %.

variation of the rotation angle differ due to systematic errors in the fit procedure.

The energy resolution for the combined energy spectrum at XENON100 for an energy of 511 keV is 2.7 % [52]. The XENON100 experiments has a better energy resolution than XAMS since it has a higher light yield than XAMS. As a result, more photons of the S1 signal are detected at XENON100, which gives a better measure for the anti-correlation of the S1 and the S2 signal.

The combined energy scale with the best resolution can be compared to the Monte Carlo simulation. Since the simulation does not take into account the finite energy resolution of the liquid xenon as scintillation material, the delta peak of the energy deposit in the liquid xenon of the simulation has to be smeared out according to the actual energy resolution of the XAMS TPC. The energy resolution for xenon TPCs is energy dependent and goes like:

$$\frac{\sigma_E}{E} = \frac{\sigma_0}{\sqrt{E}} \oplus \sigma_1, \quad (18)$$

where σ_0 and σ_1 are constants. For the combined energy scale, σ_1 is compatible with zero [52]. For each simulated energy, this gives a smeared out gaussian with an energy dependent width σ_E . Figure 43(b) shows the energy spectrum from the simulation and the best combined energy spectrum with the resolution of 4.9%. Both spectra show a photopeak at 511 keV and the corresponding Compton edge at lower energies and are in good agreement.

6 Conclusion and outlook

With this thesis XAMS has shown to be a fully operational dual-phase xenon time projection chamber, that can be deployed for detector R&D research in order to contribute to the dark matter searches of the XENON1T and future XENON experiments. The dual-phase xenon time projection chamber XAMS has an active volume containing 0.434 kg of liquid xenon, two PMTs for light detection and a fully functional cylindrical capacitance sensor that allows to measure the level of the liquid xenon with a precision of 0.12 mm. The PMTs are read out with a V1730 CAEN digitizer, that runs with the XENON1T readout software Kodiaq and the XENON1T data processor pax, which is developed at Nikhef. For the electronic recoil calibration of the detector a 370 kBq ^{22}Na source and a 6.7 kBq ^{137}Cs source are deployed. The ^{22}Na is part of a collimator setup, that allows to scan the XAMS TPC with 511 keV γ -rays at different heights. The width of the collimated γ -ray beam is 1.1 cm.

At XAMS the electron diffusion constant in liquid xenon at a field of 0.6 kV cm^{-1} was measured to be $D_L = (6.9 \pm 0.1) \times 10^{-4} \text{ mm}^2/\mu\text{s}$. A calculation of the electron lifetime showed, that after purifying xenon for three days, less than 32 % of the electrons get absorbed by impurities. Additionally, the study of the electron lifetime gave a correction factor for the S2 signal of $S2(0, E) = 25747 \pm 100 \text{ pe}$. A light collection efficiency map was calculated from a z -scan of the TPC with the collimator setup. The correction function allows to retrieve the volume averaged S1 light yield for XAMS of $0.73 \pm 0.03 \text{ pe/keV}$, which is a factor 2.67 smaller than the light yield of XENON100. The reason for the difference lies in the different geometry of the experiments. Finally, the energy resolution of the combined energy scale of the XAMS experiment was measured to be $\frac{\sigma_E}{E} = 4.9 \pm 0.1 \%$ at an incident γ -ray energy of 511 keV. The energy resolution of the XENON100 experiment is a factor 1.8 better, which is due to its different geometry. A Geant4 simulation of the collimator setup with the ^{22}Na source showed an excellent agreement with the measured event rate, γ -ray beam width and energy spectrum. For further research, XAMS requires a nuclear recoil calibration which can be achieved with a neutron source.

The quality of the calibration data is mainly limited by two factors, both connected to the height of the liquid level in the time projection chamber. Currently, the height of the level in the detector is controlled by varying the flow of the gas in the recirculation system with an extremely sensitive needle valve. This makes it difficult to reliably reproduce a certain liquid level. To obtain a secure control over the liquid level, the time projection chamber could be embedded in a diving bell construction like in the XENON experiments. In addition, the level meter readout has shown unpredicted behaviour which could be overcome by deploying a UTI microprocessor chip as readout electronic instead of an Arduino board. Research opportunities for XAMS lie in several different fields. For light detection the XENON experiments currently deploy PMTs. In order to increase the sensitivity to small signals, new light detection devices like silicon PMs are getting more and more attention. The test of these devices for the deployment at the XENON experiments is still ongoing and XAMS could engage in further research. The high sampling speed of the digitizer and the fast response of the PMTs make XAMS especially suited for the study of pulse shape discrimination for background reduction at the XENON1T experiment. The shape of the S1 pulse differs for electronic and nuclear recoils. For liquid

xenon as scintillation material, this difference is very small and it has not yet been studied in detail at low energies yet. Determining properties on the pulse shape of the S1 signal would give the XENON collaboration a second, powerful handle on the discrimination between background and signal which could lead to the discovery of the first directly detected dark matter signal.

References

- [1] NASA. http://www.nasa.gov/mission_pages/planck/news/planck20130321.html#.VNeDHS1-8b0. retrieved at 22.04.2015.
- [2] Steigman *et al.* Precise Relic WIMP Abundance and its Impact on Searches for Dark Matter Annihilation. arXiv: 1204.3622.
- [3] D. J. Adams *et al.* *An Introduction to Galaxies and Cosmology*. Cambridge University Press, 2007.
- [4] Hubble Space Telescope. <http://www.spacetelescope.org/images/potw1032a/>. retrieved at 22.04.2015.
- [5] K. *et al.* Begeman. Extended rotation curves of spiral galaxies - Dark haloes and modified dynamics. *Monthly Notices of the Royal Astronomical Society*, 249:p. 523–537, 1991.
- [6] V. Rubin, N. Thonnard, and W. Ford. Extended rotation curves of high-luminosity spiral galaxies. IV - Systematic dynamical properties, SA through SC. *Astrophysical Journal, Part 2 - Letters to the Editor*, 225:p. L107–L111, 1978.
- [7] NASA/ESA, Hubble Space Telescope. <http://www.spacetelescope.org/images/heic0910b/>. retrieved at 22.04.2015.
- [8] NASA, M. *et al.* Markevitch, and Magellan/Arizona/Clowe *et al.* <http://apod.nasa.gov/apod/ap060824.html>. retrieved at 22.04.2015.
- [9] Rolf Schoen. XAMS - development of liquid xenon detector technology for dark matter searches, 2015. PhD thesis.
- [10] D. Fixsen. The temperature of the cosmic microwave background. *Astrophysical Journal*, 707:919, 2009.
- [11] NASA. <http://wmap.gsfc.nasa.gov/media/ContentMedia/990015b.jpg>. retrieved at 22.04.2015.
- [12] ESA and the Planck collaboration. http://www.esa.int/spaceinimages/Images/2013/03/Planck_CMB. retrieved at 22.04.2015.
- [13] Planck collaboration. Planck results 2013, XV. CMB power spectra and likelihood, 2013. arXiv: 1303.5075.
- [14] Planck collaboration. Planck 2015 results. XIII. Cosmological parameters, 2015. arXiv:1502.01589.
- [15] R. D. Peccei and H. R. Quinn. CP Conservation in the Presence of Pseudoparticles. *Phys. Rev. Lett*, 38, 1977.
- [16] Roberto D. Peccei. *The Strong CP Problem and Axions*. Springer Berlin Heidelberg, 741 edition, 2008.

- [17] S. Weinberg. A New Light Boson? *Phys. Rev. Lett*, 40, 1978.
- [18] ADMX - the Axion Dark Matter eXperiment. <http://depts.washington.edu/admx/experiment.html>. retrieved at 28.04.2015.
- [19] David B. Tanner. ADMX enters its second generation, 2013. Presentation.
- [20] M. Drees and G. Gerbier. Mini Review of Dark Matter, 2012. arXiv: 1204.2373.
- [21] G. Bertone. The moment of truth for WIMP dark matter, 2010. arXiv: 1011.3532v1.
- [22] J. Jo Bovy and S. Tremaine. On the local dark matter density, 2012. arXiv: 1205.4033.
- [23] http://www.mpi-hd.mpg.de/lin/images/research_theory5.png. retrieved at 28.04.2015.
- [24] M. Buckley *et al.* Search for Gamma-ray Emission from Dark Matter Annihilation in the Large Magellanic Cloud with the Fermi Large Area Telescope, 2015. arXiv: 1502.01020.
- [25] M. Buckley *et al.* Jungman, G. and Kamionkowski, M. and K. Griest, 1995. arXiv:hep-ph/9506380.
- [26] Dr. Andrew Brown. XENON searches for dark matter, 2015. NIKHEF seminar.
- [27] Guillaume Plante. The XENON100 Dark Matter Experiment: Design, Construction, Calibration and 2010 Search Results with Improved Measurement of the Scintillation Response of Liquid Xenon to Low-Energy Nuclear Recoils, 2012. PhD thesis.
- [28] Laura Baudis. WIMP Dark Matter Direct-Detection Searches in Noble Gases, 2014. arXiv:1408.4371.
- [29] E. Aprile, A. Bolotnikov, A. Bolozdynya, and T. Doke. *Noble Gas Detectors*. Wiley, 2006.
- [30] A. Hitachi, T. Takahashi, N. Funayama, K. Masuda, J. Kikuchi, and T. Doke. Effect of ionization density on the time dependence of luminescence from liquid argon and xenon, 1983. *Phys. Rev. B* 27, 5279-5285.
- [31] Guillaume Plante. Status of the XENON Dark Matter Project: Recent Results from XENON100 and Prospects for Detection with XENON1T, 2014. Presentation.
- [32] Aprile *et al.* Dark Matter Results from 225 Live Days of XENON100 Data, 2013. arXiv: 1207.5988.
- [33] William M. Haynes, editor. *CRC Handbook of Chemistry and Physics*. CRC Press, 95th edition edition, 2014.
- [34] WS Hampshire Inc. http://catalog.wshampshire.com/Asset/psg_teflon_ptfe.pdf. retrieved at 26.04.2015.

- [35] D.Lide, editor. *CRC Handbook of Chemistry and Physics*. CRC Press, 76th edition edition, 1995-6.
- [36] C. Silva *et al.* Reflectance of Polytetrafluoroethylene (PTFE) for Xenon Scintillation Light, 2009. arXiv: 0910.1056.
- [37] S. Cherry. *PET: Physics, Instrumentation, and Scanners*. Springer, 2006.
- [38] Erik Hogenbirk. Development, commissioning and first results of XAMS - A dual-phase xenon time projection chamber at Nikhef. Master's thesis, Vrije Universiteit Amsterdam, 2014.
- [39] Hamamatsu. *Photomultiplier Tubes and Assemblies - For Scintillation Counting and High Energy Physics*, 2012.
- [40] Faan Langelaan. The XAMS level meter and pressure safety system, 2014. Bachelor's thesis.
- [41] G. Bakale, U. Sowadaand, and W. F. Schmidt. *J. Phys. Chem.* 80 (1976) 2556.
- [42] A. Baldini *et al.* (MEG Collaboration). *Nucl. Instr. Meth. Phys. Res. Sect. A* 545 (2005) 753.
- [43] CAEN. *User Manual UM2792, VI730 & VX1730, 16/8-channel 14-bit 500MS/s Waveform Digitizer*, 2014.
- [44] Bram Schermer. Testing the data acquisition of XAMS using a waveform generator., 2015. Bachelor's thesis.
- [45] Richard B. Firestone. *Table of Isotopes*. Wiley, CD ROM Edition, Version 1.0 edition, 1996.
- [46] National Institute of Standards and Technology. <http://www.nist.gov/pml/data/xcom/index.cfm>. retrieved at 17.05.15.
- [47] Official Geant4 website. <http://geant4.cern.ch>. retrieved at 06.06.15.
- [48] CERN TWiki. <https://twiki.cern.ch/twiki/bin/view/Geant4/LoweMigratedLivermore>. CERN TWiki, retrieved 03.05.2015.
- [49] Peter Sorensen. Anisotropic diffusion of electrons in liquid xenon with application to improving the sensitivity of direct dark matter searches, 2011. arXiv: 1102.2865v2.
- [50] Sebastian Lindemann. Intrinsic ^{85}Kr and ^{222}Rn Backgrounds in the XENON Dark Matter Search, 2013. PhD thesis.
- [51] J. *et al.* Allison. Geant4 Developments and Applications, 2006. *IEEE Transactions on Nuclear Science* 53 No. 1,270-278.
- [52] XENON collaboration. The XENON100 Dark Matter Experiment, 2012. arXiv: 1107.2155v2.

Acknowledgements

Within one year, I gained a tremendous amount of knowledge about the detector R&D of dark matter experiments and the physics behind the search for dark matter. I'm especially grateful to Patrick Decowski and Auke-Pieter Colijn for choosing me for this challenging, but incredible insightful Master project. I'm not only grateful for your inspiring supervision, but also for your guidance towards a career in science. I'd like to thank the kind members of the Dark Matter group for their support and input and definitely for constantly volunteering for shifts while XAMS was running. Furthermore, I'd like to thank the people in the Detector R&D group and all the other people at Nikhef, who have helped me with their technical expertise. Erik Hogenbirk, thank you for being a great supervisor, I appreciate all the time you had for discussions and explanations. Thanks to my friends and family who are still here, even though I tend to burry myself in work and most importantly: Thank you Alexander, for moving abroad and taking this journey together with me. I would not be where I am today without you.

